Simulation of cooling in a magma chamber: Implications for geothermal fields of southern Peru

Johan González [a,b], Carlos E. Zambra [a,*], Luciano González [c], Benjamin Clausen [d], Diego A. Vasco [e]

[a] Departamento de Tecnologías Industriales, Faculty of Engineering, Universidad de Talca, Curicó, Chile
[b] Doctorado en Sistemas de Ingeniería, Faculty of Engineering, Universidad de Talca, Curicó, Chile
[c] Instituto de Investigación en Geociencia, Universidad de Montemorelos, Montemorelos, México
[d] Geoscience Research Institute and Loma Linda University, Loma Linda, CA 92350, USA
[e] Departamento de Ingeniería Mecánica, Universidad de Santiago de Chile, USACH, Av. Bernardo O'Higgins 3363, Santiago de Chile, Chile

ARTICLE INFO

ABSTRACT

Numerical simulations of a geothermal reservoir often assume that the primary heat source is a magmatic system; however, heat from the host rock and the coupled complex transport phenomena between magma chamber and host rock also need to be considered. This research numerically simulated the cooling history of an enclosed magma chamber and the thermal effects on the host rock around it from which geothermal energy could be extracted. Modeling of the magma body included natural convection, the effect of latent heat of phase change when the crystals are being formed between the liquidus temperature and the solidus temperature, and heat conduction when the temperature is below the solidus temperature. This study takes as an example a geothermal reservoir in southern Peru (Western Cordillera) whose heat source is a rhyolitic magma chamber like those that gave rise to the intrusive rocks of the Peru coastal cordillera. This analysis varies the chamber shape and uses three solidification temperature ranges for convection and conduction models above the rock formation temperature (solidus) to study the implications for heating of the host rock. This is the first study of its kind in this area. The center of an average-sized magma chambers takes approximately 500 ka to cool from 800 °C to 300 °C. Simulated cooling times between intrusion and solidus temperatures decreased 3 ka when convection was modeled along with conduction cooling. Cooling times decreased by up to 6 ka when the solidification temperature range was increased. The host rock temperature pattern depends strongly on the stage at which the magma chamber is modeled to begin cooling. The temperatures results near the surface of the host rock obtained in this work match well with measurements at hot springs founded in several places in the Western Cordillera. Application of the methodology proposed in this study can reduce uncertainties in planning geothermal energy extraction wells. The accuracy of the numerical model described here could be improved by including more ground data from exploration wells, e.g., soil stratigraphy and temperatures variation with depth.

1. Introduction

Energy can be delivered to hydrothermal systems from various heat sources (Lund, 2007), but magma chambers are considered to be the primary heat source for geothermal energy (Davies and Davies, 2010; González-Acevedo and García-Zarate, 2019). To best develop this energy resource, many factors need to be taken into account in modeling the geothermal system, e.g., the magma composition and temperature, magma convection, the thermal history, and the host rock as well as the chamber. In this study, these factors are taken into account in modeling a geothermal reservoir, using southern Peru as the example with geothermal potential.

Magmas have different geochemical compositions (Chappell, 1996) and the crystallization temperature range varies with the composition (Nelson, 2011). Thus, knowing the geochemical composition is necessary for simulating the magma crystallization and the temperature distribution in the host rock. Various authors, e.g., Nelson (2011), indicate a range of 650−850°C for crystallization of felsic rhyolitic magmas. This

paper studies the effect of crystallization temperature range on the cooling of a magma chamber and its effect on the host rock.

Convection in an enclosed magma chamber is due to natural heating from below, i.e., heat flow from the earth's core and cooling from above (Bartlett, 1969; Shaw, 1965). Magmas have a range of temperatures and chemical compositions that produce a non-Newtonian behavior for viscosity (Sparks et al., 1984; Zambra et al., 2022), while other transport properties such as density, specific heat and conductivity vary little with the temperature (Lesher and Spera, 2015). These considerations were included in our simulations of magma cooling before solidification within three shapes of magma chambers.

An understanding of geothermal areas, as well as geological plutons and batholiths and mineral formation, requires a knowledge of the thermal history. This is dependent on igneous intrusions that alter the temperature profile in the surrounding host rock and on the water temperature of underground aquifers. This thermal history has been extensively investigated in different geological contexts such as petrology (e.g., Keller and Suckale, 2019), petroleum geology (e.g., Fjeldskaar et al., 2008), epithermal ore deposits (e.g., Sparks et al., 2019), coal geology (e.g., Guo et al., 2019), contact metamorphism (e.g., Douglas et al., 2016; Iyer et al., 2018), organic geochemistry (e.g., Liu and Jiang, 2019) and geothermal reservoirs (Fu et al., 2010).

When developing computational models of geothermal sites, it is common to apply a heat source to represent the magmatic system providing the energy (Deb et al., 2021; Espinoza-Ojeda et al., 2021). The resulting numerical model ignores the historical cooling of the magma chamber and the transport processes that occur inside it. Such a model has inaccuracies that affect the temperature evolution in both the chamber and the host rock. This study presents coupled simulations of magma chamber and host rock, with an emphasis on magma transport phenomena, i.e., movement, heat flow, phase change, crystallization temperature range and chamber shape, that can affect temperatures of a geothermal system.

Calderas at earth's surface indicate heat sources beneath (Gudmundsson, 2012) with the potential for generating geothermal energy from high-enthalpy resources within drillable depths. The study area in this work is located in the Western Cordillera of Peru where several active Quaternary calderas are found in the southern Peruvian volcanic belt. The Moquegua basin between the Western Cordillera and Coastal Cordillera can provide information about the stratigraphy around the geothermal reservoirs. No data from test boreholes for geothermal prospecting are available on stratigraphy and temperature variations in this area. Instead, temperature data from the hot springs are used as a reference for comparing the results obtained with our numerical simulations. The current magma chambers that could be sources of geothermal reservoirs may be like those that gave rise to the Peruvian Coastal Batholith (PCB) at the western boundary of the basin. Information collected in geological studies of the PCB (e.g., Agar, 1981; Haederle and Atherton, 2002; Lamy-Chappuis et al., 2020) is used to build a conceptual model which is simulated computationally. These analyses in conjunction with field data may support the selection of optimal geothermal energy extraction points. In short, we integrate the accepted geological model for a magma chamber that forms a pluton in the PCB with the available stratigraphic data in the Moquegua basin to simulate the largest geothermal reservoir in Peru.

The paper is organized as follow: First, available geological information relevant to the study area and the conceptual model proposed for the simulations are presented in Section 2. Then, section 3 describes the mathematical model used to reproduce the cooling history of the magma in the chamber and its effects on the heat flow in the host rock. The computational procedure, accuracy tests that include a mesh study and the algorithm validation are develop in Section 4. Based on the conceptual model built for a geothermal zone located in the Western Cordillera next to the Moquegua Basin, the numerical simulations produced by the proposed model are presented and discussed in Section 5.

2. Background

Peru has great potential for geothermal energy; however, no geothermal power plant has been developed and no one company has drilled any geothermal wells (exploratory or slim holes) (Cruz Pauccara and Guardia, 2015). Several studies have been carried out in the last decade with the purpose of characterizing and evaluating the geothermal potential (Cruz et al., 2013; Japan International Cooperation Agency, 2012). It is estimated that the geothermal potential in the country in around 3000 MW, where more than 57% of the most promising fields are located in the Western Cordillera of southern Peru, in the Arequipa, Moquegua, and Tacna Provinces (Japan International Cooperation Agency, 2012).

The Moquegua basin covers a large part of these three provinces (see Fig. 1a); therefore, its composition and evolution are important for the definition of our conceptual model. Subduction of the Nazca plate under South America and the resulting magmatism and large Andean uplift are a dominant Cenozoic process, but they started much earlier and continue to the present. Subduction produced extensive deformation as well as volcanic andesites and plutonic batholiths (Cruz Pauccara and Guardia, 2015). In southern Peru this geological environment with active volcanism results in great geothermal potential (Cruz Pauccara and Guardia, 2015). This geological activity in the western cordillera branch of the Andes, especially the southern section of the Peruvian Coastal Batholith, caused sedimentary landslides (sandstone) during the
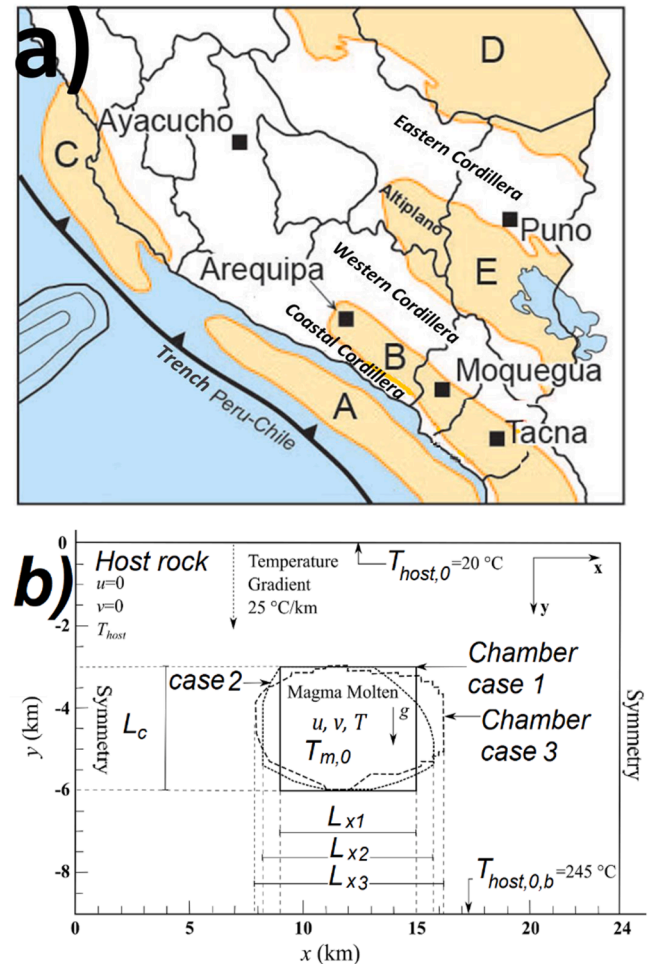

Fig. 1. (a) Position of the Moquegua sedimentary Basin (B) in relation to the other Cenozoic basins (A: Camaná-Molledo Basin; C: Pisco Basin; D:Madre de Dios Basin; E: Titicaca Basin) of southern Peru (Alván et al., 2020); (b) conceptual model for the three magma chamber shapes studied.

Eocene-Pliocene in the basins of southern Peru. This is particularly true for the Moquegua sedimentary basin where Peru's largest geothermal reserves are located (Japan International Cooperation Agency, 2012). The basement of the Moquegua Basin is composed mainly of basaltic andesites of the Lower Jurassic (Alván et al., 2020). Since the beginning of the Cenozoic, a stratigraphic thickness of at least 800 m of sediments has accumulated in the Moquegua basin in a fluvial and lacustrine environment, accompanied by calc-alkaline pyroclastic volcanics. The sediments are primarily sandstone (Alván, 2020).

The Western Coastal Cordillera of Peru includes the Peruvian Coastal Batholith (PCB) which extends over 1600 km and is the major plutonic phase of Mesozoic magmatism in Peru (Haederle,2002). The northern and southern PCB contain intrusive rocks with a high-silica geochemical composition originating from magma of andesitic to rhyolitic composition. Several examples along the PCB of intrusive rocks with a geochemical composition near that of a rhyolitic magma are associated with hot springs. Here are two examples. In the northern section of the PCB, in the Tectahuayin, Oyon province, Lima department plutons are found having a tonalite composition intermediate between andesite and rhyolite (Cobbing and Garayar, 1998). This area has multiple hot springs and its geothermal potential is estimated at 21-60 MW (Cruz Pauccara and Guardia, 2015). In the southern section of the PCB, near the city of Arequipa (Coastal Cordillera in Fig. 1a), several felsic intrusive rocks are also found on geologic maps, e.g., tonalite of Torconta (KTi-tot), tonalite of Laderas (KTi-tol) and granodiorite (KTi-gd) which cover about 300 km^2 (Vargas and Del Pino, 1995). Since felsic rhyolitic magma chambers have existed in the area, it is possible that heat source for geothermal reservoirs there are chambers containing rhyolitic magma.

Several authors have suggested that the plutons of the PCB are commonly 5.0 km thick or less, and 4-10 km wide in certain sections (Couch et al., 1981; Haederle and Atherton, 2002). Analysis of saline inclusions in the PCB Linga complex suggest magma crystallization pressures between 800 and 900 bar, indicating that the depth from the surface to the top of the magma chamber in the Earth's crust lies between 2.9 and 3.2 km from the surface of the earth when crystallizing (Agar, 1981; Lamy-Chappuis et al., 2020).

In summary, geological studies have been carried out in southern Peru, which has 13 geothermal zones of interest (Barragán et al., 1999; Cruz et al., 2013). The studies indicate that the main heat source is magma chambers such as those that feed the volcanoes of the western mountain range where the heat flux varies between 110 and 235 mW/m^2 (Hamza et al., 2005). In this area, an 800m-thick sediment layer composed primarily of sandstone overlies basaltic andesitic. The conceptual model was developed based on these considerations about the geological structure of the region. Fig. 1a shows the area of this study and Fig. 1b shows the conceptual model with three magma chamber shapes for the cases studied.

2.1. Conceptual model

Based on information presented in the previous section we propose a conceptual model for a geothermal area located in southern Peru. The geological structure suggests a magma chamber surrounded by host rock made up of sandstone down to 800 m depth and low permeability basaltic andesite beneath to 9000m depth. Magma chamber shape and size are two key parameters that determine heat flow. The shape and depth of the simulated chamber were estimated from geological studies of magma chambers making up the PCB (Agar, 1981; Couch et al., 1981; Haederle and Atherton, 2002). In the simulations, the top of the chamber is located at 3.0 km depth from the surface while the maximum chamber thickness is taken as 3.0 km ($L_c = 3000$ m) (see Fig. 1b).

In general, magma chambers that formed a pluton in the PCB have a tabular shape, i.e., the thickness is less than the width (Haederle and Atherton, 2002). In addition, pluton emplacement in this batholith involves regional tilting, stoping, and a combined cantilever/piston mechanism which can produce irregularities at the edges of the chamber

(Haederle and Atherton, 2002). The three different shapes for magma chambers used in our simulations are based on studies by Haederle and Atherton (2002) and Cruden (1998). The simulated chamber shapes are described in Fig. 1b: rectangular (case 1_SQ), a mixed shape between rectangular and elliptical called in this study hybrid (case 2_HI), and quasi-elliptical (case 3_QU). In order to compare results, all simulated chamber shapes have the same area of 18 km^2, which is obtained by varying the width of the chamber (case 1: $L_{x1} = 6.0$ km, case 2: $L_{x2} = 7.5$ km, and case 3: $L_{x3} = 8.375$ km). Fig. 1b presents the conceptual model used for simulations, showing the three cases with three different chamber shapes.

Several numerical simulations using conduction models have been used to study the heat flow and melt fraction in sill-like magma chambers and to describe the effects on the temperature of the host rock (Douglas et al., 2016; Fjeldskaar et al., 2008; Wang et al., 2012). We are including convection as well. Magma velocities increase markedly with the size of the chamber and can become the dominant method of heat transfer and distribution of crystals inside it (Lamy-Chappuis et al., 2020). For our simulation, the magma inside the chamber has an initial convection velocity of zero in both coordinates and an initial temperature, $T_{m,0}$, of 800 °C.

An average value for the heat flow from the Earth's mantle is $Q = 60$ mW/m^2 (Yoshinobu et al., 1998). This value is commonly used in the literature to produce a geothermal temperature gradient of 25°C/km in the crust (Lowell et al., 2014), which is considered in this work as the initial temperature variation in the host rock. Initial temperature at the surface is $T_{host,0} = 20$°C and at -9 km of depth $T_{host,0,b} = 245$°C.

The geothermal heat source is taken to be a rhyolite magma (Vargas and Del Pino, 1995) that intruded into the crust forming a chamber that then became a closed system (Cruz Pauccara and Guardia, 2015; Japan International Cooperation Agency, 2012). No uplifting or exhumation of the magma chamber in the host rock occurs during cooling.

3. Mathematical model and numerical simulation

3.1. Geological setting and mathematical model for the intrusion

This sub-section presents the two-dimensional mathematical approach for modeling magma cooling by convection and the geological aspects involved. High magma chamber temperature coupled with low host rock temperature are sufficient to produce convection in the magma, even if it has a high Prandtl number (Bartlett, 1969). The magma in the chamber is subject to a particular type of natural convection called Rayleigh-Bernard (RB) convection (Eckert et al., 1988) due to heat flowing from the core of the earth that produces a high temperature at the bottom edge of the magmatic body in contrast with a lower temperature at the top edge. The coupled system of partial differential equations that reproduces the movement and cooling of magmas includes mass conservation, momentum, and energy. The mass conservation and momentum equations are given by:

$$\frac{\partial u_m}{\partial x} + \frac{\partial v_m}{\partial y} = 0 \tag{1}$$

$$\rho_m \left[\frac{\partial u_m}{\partial t} + u_m \frac{\partial u_m}{\partial x} + v_m \frac{\partial u_m}{\partial y} \right] = -\frac{\partial p_m}{\partial x} + \eta_m \left[\frac{\partial u_m}{\partial x} + \frac{\partial u_m}{\partial y} \right] \tag{2}$$

$$\rho_m \left[\frac{\partial v_m}{\partial t} + u_m \frac{\partial v_m}{\partial x} + v_m \frac{\partial v_m}{\partial y} \right] = -\frac{\partial p_m}{\partial y} + \eta_m \left[\frac{\partial v_m}{\partial x} + \frac{\partial v_m}{\partial y} \right] + \rho_m g \beta \left(T - T_{ref} \right) \tag{3}$$

where x and y are the spatial coordinates, u and v are the velocity in the x and y directions respectively, ρ_m is the density, t is the time, p_m is the pressure, g is the gravitational acceleration, β is the thermal expansion coefficient and η_m is the viscosity. The subscripts m and ref, represent the properties for the magma intrusion and the reference temperature, respectively. The momentum Eq. (3) includes the buoyancy term in the

y-direction. The relation between density and pressure is simplified by applying the Oberbeck-Boussinesq approximation (Ahlers et al., 2009), which means that density only depends on temperature and hence the flow is incompressible. The convection-conduction equation for melt is as follow:

$$\rho_m Cp_m \left[\frac{\partial T_m}{\partial t} + u_m \frac{\partial T_m}{\partial x} + v_m \frac{\partial T_m}{\partial y} \right] = k_m \left[\frac{\partial^2 T_m}{\partial x^2} + \frac{\partial^2 T_m}{\partial y^2} \right] \quad (4)$$

where T_m is the temperature, Cp_m is the heat capacity, and k_m is the thermal conductivity. It is assumed that thermal radiation is negligible. A similar system of equations Eqs. (1)−((4)) was applied by Rabbani-pour Esfahani et al. (2018) for turbulent thermal convection.

3.2. Phase change fraction equations for magma

In this work, we include the widely-accepted mathematical phase change fraction model (Galushkin, 1997). During cooling, the melt passes through several phases: liquid above the liquidus temperature, liquid-solid mixture (mushy zone) between liquidus and solidus temperatures, and solid below the solidus temperature. As a result, the following subscripts will be assigned to the properties of the intrusion for each phase: *l* liquid, *pc* phase change, and *s* solid. In the phase change fraction of the model, heat capacity (Cp_{pc}), density (ρ_{pc}), thermal conductivity (k_{pc}), and apparent viscosity (η_{pc}) are modified as a function of the phase change fraction (f_{pc}) (Galushkin, 1997; Moraga et al., 2010) as follows:

$$Cp_{pc} = \left(Cp_l + \frac{L_m}{(T_{lus} - T_{sus})} \right) f_{pc} + \left(Cp_s + \frac{L_m}{(T_{lus} - T_{sus})} \right) (1 - f_{pc}) \quad (5)$$

$$\rho_{pc} = \rho_l f_{pc} + \rho_s (1 - f_{pc}) \quad (6)$$

$$k_{pc} = k_l f_{pc} + k_s (1 - f_{pc}) \quad (7)$$

$$\eta_{pc} = \eta_l f_{pc} + \eta_s (1 - f_{pc})^{10} \quad (8)$$

where L_m is the latent heat of phase change of the magma and T_{lus} and T_{sus} are the liquidus temperature (when the first solid crystal appears) and the solidus temperature (when the last drop of liquid is solidified). Symbols for magma in the liquid state are: heat capacity (Cp_l), density (ρ_l), thermal conductivity (k_l) and viscosity (η_l). Symbols for magma in the solid state are: heat capacity (Cp_s), density (ρ_s), thermal conductivity (k_s) and viscosity (η_s). The properties used in this paper for rhyolite magma simulations are shown in Table 1. The phase change fraction f_{pc}, is calculated as a function of the temperature of the melt:

$$f_{pc} = \begin{cases} 1 & T_m \geq T_{lus} \\ \frac{T_m - T_{sus}}{T_{lus} - T_{sus}} \Rightarrow \quad if \Rightarrow \quad T_{sus} < T_m < T_{lus} \\ 0 & T_m \leq T_{sus} \end{cases} \quad (9)$$

Magma composition varies depending on the percentage of Earth's major elements. The range results from a combination of original mafic mantle melts, magma differentiation, and contamination from felsic crustal melt (Chappell, 1996). The result is a large range of magma viscosities that affect magma movement (convection) which in turn influences magma cooling rates and the heat flowing to the host rock. Several experiments have shown that the magma behaves like a Bingham or pseudoplastic fluid (Ryerson et al., 1988; Shaw et al., 1968) whose apparent viscosity can use an Arrhenius model (Lesher and Spera, 2015; Ni et al., 2015; Sonder et al., 2006). In some mathematical models and numerical simulations, the non-Newtonian behavior of the melt is not taken into account for the sake of simplicity (González Oli-vares, 2017; Rabbanipour Esfahani et al., 2018; Yoshinobu et al., 1998); however in this paper we use an Arrhenius type equation to calculate the

Table 1
Rhyolite properties used in the mathematical model for the melt and host rock.

Symbol	Meaning	Units	Value	Refs.
Cp_l	Specific heat of magma in liquid state	J kg$^{-1\circ}$C^{-1}	1338.692	(Lesher and Spera, 2015)
Cp_s	Specific heat of magma in solid state	J kg$^{-1\circ}$C^{-1}	807.652	(Lesher and Spera, 2015)
Cp_{matrix}	Specific heat of rock matrix of host rock	J kg$^{-1\circ}$C^{-1}	1000.0	(Yoshinobu et al., 1998)
Cp_w	Specific heat of pore water	J kg$^{-1\circ}$C^{-1}	4181.30	(Wang et al., 2012a)
k_l	Thermal conductivity of magma in liquid state	W m$^{-1\circ}$C^{-1}	1.50	(Lesher and Spera, 2015)
k_s	Thermal conductivity of magma in solid state	W m$^{-1\circ}$C^{-1}	3.30	(Lesher and Spera, 2015)
$k_{matrix,2}$	Thermal conductivity of low permeability matrix in the host rock (at 800-9000m depth)	W m$^{-1\circ}$C^{-1}	2.65	(Yoshinobu et al., 1998)
$k_{matrix,1}$	Thermal conductivity of sandstone matrix in the host rock (at 0-800m depth)	W m$^{-1\circ}$C^{-1}	2.8	(Hamza et al., 2005)
k_w	Thermal conductivity of pore water	W m$^{-1\circ}$C^{-1}	0.58	(Wang et al., 2012)
L_m	Latent heat of magma	J kg^{-1}	2200E3	(Lesher and Spera, 2015)
L_d	Average latent heat of dehydratation and decarbonation reactions	kJ/kg	170	(Galushkin, 1997)
L_v	Latent evaporation heat of pore water	kJ/kg	1398	(Wang et al., 2012)
L_c	Caracteristic length	m	3000	
T_{boil}	Boiling point of water in host rock	°C	302.5	(Wang et al., 2012)
ρ_l	Density of magma in liquid state	kg m^{-3}	2444.273	(Lesher and Spera, 2015)
ρ_s	Density of magma in solid state	kg m^{-3}	2600	(Lesher and Spera, 2015)
ρ_{matrix}	Density of host rock	kg m^{-3}	2670	(Yoshinobu et al., 1998)
ρ_w	Density of water in the porous media	kg m^{-3}	1000	(Wang et al., 2012)
ϕ	Porosity of the host rock	-	0.2 (Sandstone) 0.05 (Franctured igneous and metamorphic rocks)	(Sanders, 1998)
ΔT_d	difference between the lower and the upper limit of the temperature of dehydration and decarbonation reactions	°C	300	(Wang et al., 2012)
ΔT_v	difference between the lower and the upper limit of the temperature of pore-water evaporation	°C	5	(Wang et al., 2012)
η_l	Apparent viscosity of magma in liquid state	Pa s		(Lesher and Spera, 2015)
η_0	Asymptotic viscosity of magma as $T \to \infty$	Pa s	1E-5.6	(Lesher and Spera, 2015)
η_s	Viscosity of magma in solid state	Pa s	1.E30	
β_T	Thermal expansion coefficient	K^{-1}	0.000877826	(Lesher and Spera, 2015)

viscosity variation (η_l) in the magma (rhyolite) as a function of temperature (Lesher and Spera, 2015) during the formation of crystals. This equation can be used for a temperature range of 925−700°C (Lesher and Spera, 2015):

$$\eta_l = \eta_0 \exp[(E_A + P_m V_A) / RT_m] \tag{10}$$

In this equation η_0 is the asymptotic viscosity as $T{\to}\infty$(1E-5.6), E_A is the activation energy for viscous flow (3E5 J/mol), P_m is the mean lithostatic pressure of magma (8.5E7 Pa), R is the universal gas constant (8.31451 J/mol K), V_A is the activation volume (3E-6 m^3/mol), and T_m is the average temperature of the magma. Other thermophysical properties used for simulations are presented in Table 1.

3.3. Conduction in porous media in the host rock

Heat conduction models have been used successfully in several papers to reconstruct the thermal history of low permeability host rocks (e. g., $\leq 10^{-16}$m^2) (Galushkin, 1997; Hayba and Ingebritsen, 1997; Wang et al., 2012). To estimate the effect of magma chamber temperature on the heat flux in the host rock requires the inclusion of water effects in the host rock, such as pore-water evaporation, dehydration and decarbonation reactions. This model considers that the porous host rock is filled with water if the temperature is below T_{boil}, and the pore-water content is zero above this temperature. The heat conduction equation that includes dehydration and decarbonation reactions as presented by Wang et al. (2012) is expanded to two dimensions as follows:

$$\left(\rho_{host}Cp_{host} + \frac{L_d \rho_{matrix}(1-\phi)}{\Delta T_d} + \frac{L_v \rho_w \phi}{\Delta T_v}\right)\frac{\partial T_{host}}{\partial t} = k_{host}\left[\frac{\partial^2 T_{host}}{\partial x^2} + \frac{\partial^2 T_{host}}{\partial y^2}\right] \tag{11}$$

where ϕ is the porosity; the subscript *host* is used to indicate properties of the host rock; L_d and L_v are the average latent heat of dehydration and decarbonation reactions and the latent evaporation heat of pore water, respectively; ρ_{matrix} and ρ_w are density of rock and water, respectively; ΔT_d is the difference between the lower and upper limits of the temperature of dehydration and decarbonation reactions; and ΔT_v is the difference between the lower and upper limits of the temperature of pore-water evaporation. The values used in this work for the "before" parameters are listed in Table 1. We note that this conduction model assumes that the host rock is saturated with water, that no movement of water in the rock occurs, and that the heat loss due to volatiles escaping out of the host rock is neglected.

Since pore-water evaporation is considered in the model, the total thermal conductivity (k_{host}), specific heat (Cp_{host}), and density (ρ_{host}) of host rocks must be computed from Wang et al. (2012):

$$\rho_{host} = \begin{cases} \rho_{matrix}(1-\phi_i) & T_{host} > T_{boil} \\ \rho_{matrix}(1-\phi_i) + \rho_w\phi_i & T_{host} \leq T_{boil} \end{cases} \tag{12}$$

$$k_{host} = \begin{cases} k_{matrix,i}(1-\phi_i) & T_{host} > T_{boil} \\ k_{matrix,i}(1-\phi_i) + k_w\phi_i & T_{host} \leq T_{boil} \end{cases} \tag{13}$$

$$Cp_{host}\begin{cases} Cp_{matrix}(1-\phi_i) & T_{host} > T_{boil} \\ Cp_{matrix}(1-\phi_i) + Cp_w\phi_i & T_{host} \leq T_{boil} \end{cases} \tag{14}$$

In these equations, T_{boil} is the boiling temperature of water in the host rock and ϕ_i is the porosity. We use a variable conductivity with the matrix ($k_{matrix,i}$) and a variable porosity ϕ_i, since Section 2 noted that the host rock is primarily sandstone down to 800 m depth and fractured igneous and metamorphic rocks beneath that. Therefore, down to 800 m deep, the thermal conductivity is 2.8 W/m K ($k_{matrix,1}$) (Hamza et al., 2005) and the porosity is 0.2 (Sanders, 1998). Below that, the thermal conductivity is 2.65 W/m K ($k_{matrix,2}$) (Yoshinobu et al., 1998) and porosity decreases to 0.05 (Sanders, 1998). Nomenclature and references for host rock values used in simulations are listed in Table 1.

3.4. System of dimensionless equations

In this section, dimensionless equations are obtained by parameterizing the variables of the dimensional mathematical model. For this study, the dimensionless model improves the stability and convergence of the numerical method. In order to obtain the dimensionless mathematical model used in this simulation, the equations presented in the previous section, i.e., Eqs. (1)−(4) and Eq. (11), were parametrized. using the following expressions:

$$X = \frac{x}{L_c}; \quad Y = \frac{y}{L_c}; \quad \tau = \frac{t \cdot \alpha_l}{L_c^2}; \quad U = \frac{u_m L_c}{\alpha_l}; \quad V = \frac{v_m L_c}{\alpha_l};$$

$$\frac{p^*}{p} = \left(\rho_l\frac{\alpha_l^2}{L_c^2}\right)^{-1}; \quad \theta = \frac{T - T_{sus}}{T_{lus} - T_{sus}}; \quad Ra_T = \frac{\rho_l g \beta_T (T_{lus} - T_{sus}) \cdot (L_c)^3}{\eta_l \alpha_l} \tag{15}$$

where X and U are the dimensionless coordinates and velocity in the x direction; Y and V are the dimensionless coordinates and velocity in the y direction; α_l, ρ_l and β_T are the thermal diffusivity, density and thermal expansion coefficient of magma in the liquid state, respectively; and g is the gravitational force. The equation to parameterize the time (τ) is from Llambías (2014), who used it to determine the heat dissipation in an igneous body. The governing equations written in dimensionless form for melt inside the magma chamber become:

$$\frac{\partial U_m}{\partial X} + \frac{\partial V_m}{\partial Y} = 0 \tag{16}$$

$$\frac{\partial U_m}{\partial \tau} + U_m\frac{\partial U_m}{\partial X} + V_m\frac{\partial U_m}{\partial Y} = -\frac{\partial p_m^*}{\partial X} + Pr_m\left[\frac{\partial^2 U_m}{\partial X^2} + \frac{\partial^2 U_m}{\partial Y^2}\right] \tag{17}$$

$$\frac{\partial V_m}{\partial \tau} + U_m\frac{\partial V_m}{\partial X} + V_m\frac{\partial V_m}{\partial Y} = -\frac{\partial p_m^*}{\partial Y} - Pr_m\left[\frac{\partial^2 V_m}{\partial X^2} + \frac{\partial^2 V_m}{\partial Y^2}\right] + Pr_m \cdot Ra_{T_j}\theta \tag{18}$$

$$\frac{\partial \theta_m}{\partial \tau} + U_m\frac{\partial \theta_m}{\partial X} + V_m\frac{\partial \theta_m}{\partial Y} = \frac{\alpha_m}{\alpha_l}\left[\frac{\partial^2 \theta_m}{\partial X^2} + \frac{\partial^2 \theta_m}{\partial Y^2}\right] \tag{19}$$

The dimensionless Prandtl number for magma (Pr_m) is calculated as a function of the temperature, as follows:

$$Pr_m = \begin{cases} Pr_l = \dfrac{\eta_l}{\rho_l\alpha_l} & T \geq T_{lus} \\[2mm] Pr_{pc} = \dfrac{\eta_{pc}}{\rho_{pc}\alpha_{pc}} & T_{sus} < T < T_{lus} \end{cases} \tag{20}$$

The Prandtl number relates momentum and thermal diffusion. Magmas have high Prandtl numbers, e.g., 1E3-1E8 (Kaminski and Jaupart, 2003), indicating that the momentum diffusion is much greater than the thermal diffusion.

The global Rayleigh number (Ra_T) is used to build the dimensionless model, but in this work a local Rayleigh number is calculated in each control volume corresponding to the magma. This implies that the characteristic length L_c is calculated as a summation of length in the y direction for each control volume ($YCV_{i,j}$). This will be explained in detail later in the numerical procedure section.

The corresponding dimensionless energy equation for conduction in the host rock is:

$$\left[1 + \frac{A_{matrix} \cdot (1-\phi) \cdot L_d}{\Delta\theta_d} + \frac{A_w \cdot (1-\phi) \cdot L_v}{\Delta\theta_v}\right]\frac{\partial \theta_{host}}{\partial \tau} = \frac{\alpha_{host}}{\alpha_l}\left[\frac{\partial^2 \theta_{host}}{\partial X^2} + \frac{\partial^2 \theta_{host}}{\partial Y^2}\right]$$

$$A_{matrix} = \frac{\rho_{matrix}}{\rho_{host} \cdot Cp_{host}}; \quad A_w = \frac{\rho_w}{\rho_{host} \cdot Cp_{host}} \tag{21}$$

where α_{host} and α_l are the thermal diffusivity of the host rock and the magma in liquid state, respectively.

3.5. Initial and boundary conditions

The simulations assume that the igneous magma is instantaneously intruded into a homogeneous host rock and the temperature stays constant ($T_{m,0}$=800°C) for a time interval Δt_0=6.2 ka (dimensionless time $\Delta\tau_1$=0.01) allowing it to modify the host rock temperature. This initial

condition used by several authors (Galushkin, 1997; Wang et al., 2012a) allows the development of temperature contours in the host rock and corresponds to the case where the chamber is fed with melt (at temperature $T_{m,0}$) without changes in shape for a time (Δt_0) before closing and starting to cool. The mechanism for emplacement of magma due to the density difference between magma and host rock is not considered in this study. The computational simulation ends when the average temperature of the chamber drops to 300°C. This was observed after about 300 ky, corresponding to dimensionless time of $\tau = 0.3$.

In the host rock, only diffusion occurs, hence velocities are zero ($u = 0$ and $v = 0$). An initial temperature gradient of 25°C/km is implemented using a linear distribution A symmetry condition for lateral boundaries of the host rock in dimensionless notation is imposed as follow:

$$\left.\frac{\partial \theta_{host}}{\partial Y}\right|_{x=0} = 0; \qquad \left.\frac{\partial \theta_{host}}{\partial Y}\right|_{x=1} = 0 \tag{22}$$

4. Computational procedure and accuracy tests

4.1. Numerical procedure

The coupled partial differential equation (PDE) system is solved numerically using the finite volume method (FVM) and the SIMPLE algorithm (Patankar, 1980). This numerical method has recently been used and explained in detail for geological simulation by Espinoza-Ojeda et al. (2021). A summarized explanation is presented below. Our programmed code, written in Fortran, solves the PDE system using the generalized form for the transport equation that contains non-steady convection, diffusion, and linearized source terms.

$$\frac{\partial(\rho\varphi)}{\partial t} + div(\rho \vec{u}\varphi) = div(\Gamma \cdot grad\varphi) + Sc + Sp \cdot \varphi \tag{23}$$

An explicit Euler scheme is used to calculate the integration over time.

$$\frac{\partial \varphi}{\partial \tau} = \frac{\varphi^{\tau+\Delta\tau} - \varphi^{\tau}}{\Delta\tau} \tag{24}$$

At each time step, the system of discretized nodal equations for each main variable (U, V, θ) is solved iteratively with a combination of the alternating tridiagonal matrix algorithm (TDMA) and the Gauss-Seidel method and the SIMPLE (semi-implicit method for pressure linked equations) algorithm. This procedure uses under-relaxation coefficients of 0.25 for the velocity components U and V and 0.8 for pressure. For temperature, under relaxation was not necessary. The convergence criteria for velocity and temperature in each dimensionless time step ($\Delta\tau = 0.0005$) and for each control volume (i,j) is $|\varphi_{i,j}^{\tau} - \varphi_{i,j}^{\tau-1}| \leq 10^{-4}$. For more details about the finite volume method and the SIMPLE algorithm, consult Versteeg and Malalasekera (2007).

For the volume occupied by the host rock, no convection is assumed, and diffusion is the only heat transport mechanism. This is also applied in zones where the magma has completely solidified, that is, its temperature is below the solidus temperature (T_{lus}).

In simulations, a local Rayleigh number ($Ra_{L,T,j}$) is used to calculate the flotation term in the y-momentum equation for each control volume in the magma chamber (CV_{melt}) where there is melt. The characteristic length of the global Rayleigh number (L_c) is changed by the corresponding length of control volume in the y coordinate ($YCV_{i,j}$).

$$Ra_{L,T,j}(i,j) = \frac{\rho_l g \beta_T (T_{lus} - T_{sus}) \cdot (YCV_{i,j})^3}{\eta_l \alpha_l} \tag{25}$$

If one adds the y length of the j control volumes in any y-profile of the rectangular intrusion (case 1) or where the height of the chamber is maximum ($i = L_{imax}$) for irregular intrusions (cases 2 and 3), one obtains the general characteristic length ($L_c = 3000.0$ m) and the global Rayleigh number

$$L_c = \sum_{j=jmin}^{j=jmax} YCV_{Limax,j} \cdot L_c \tag{26}$$

for i and j in the initial CV_{melt}. Note that the local Rayleigh number is calculated at each time step and for each control volume where there is melt. The change of the characteristic length to calculate the Rayleigh number has previously been used in studies of the solidification of metals (Rad et al., 2013; Ramirez and Beckermann, 2003) and for melting of ice (Rabbanipour Esfahani et al., 2018).

The relative error (RE) calculated for the mesh and validation test are obtained with a second order trapezoidal method at time τ between referenced data and calculated results (Zambra et al., 2015). The polynomial function for the referenced data ($f(x,y)_{\tau,ref}$) and for the calculated results ($f(x,y)_{\tau,FVM}$) is obtained with the least squares method:

$$RE = \frac{\left| \int_{y=0}^{y=max} f(x,y)_{\tau,FVM} dy - \int_{y=0}^{y=max} f(x,y)_{\tau,ref} dy \right|}{\left| \int_{y=0}^{y=max} f(x,y)_{\tau,ref} dy \right|} \tag{27}$$

4.2. Mesh study

In order to optimize the calculation times and to check that mesh size will not affect the results, five meshes were compared. It was verified that the greatest velocity and temperature gradients occur in the chamber because of the natural convection of the melt, while in the host rock diffusion produces smaller gradients. For this reason, the convergence of the mesh is studied only in the magma chamber. The physical situation corresponds to a rectangular chamber surrounded by host rock at constant temperature (boundary conditions). This simplification was adopted to reach the steady state of the variables $\phi(u,v,T)$ in the magma. A constant temperature of $T = 705$°C at the top (T_{top}) and $T = 750$°C at the bottom of the chamber (T_{bottom}) was imposed during the simulations. For the lateral walls of the chamber, a linear temperature gradient between T_{top} and T_{bottom} was imposed as the initial condition at the host rock zone. An initial temperature of $T_{m,0} = 800$°C in the magma chamber was adopted. For this study, T_{lus} and T_{sus} are 725°C and 700°C, respectively. All meshes are uniform except mesh 5, which was refined in the chamber. Meshes, results and errors of this study are summarized in Table 2.

Since the driving force for natural convection is gravity (which in our mathematical model is acting on the y coordinate), it is assumed that the velocity gradients are greater in the v component of the velocity. Therefore, the mesh convergence is studied analyzing a v-profile in x-coordinate (9-15 km in Fig. 2) at a depth of 4.5 km once all variables (φ (u, v, T)) have converged ($t = 31.0$ ka). To calculate the RE, the dimensionless profiles obtained from each mesh are compared with those of the finest mesh (mesh 1). Fig. 2 shows the behavior of the v-velocity profile at 4.5 km depth.

The results of the other meshes converge towards the result of the densest mesh. Mesh 2 and mesh 5 have similar values of REs and the lowest calculated, but mesh 5 has fewer nodes. Therefore, a non-uniform mesh of 88×44 nodes in the chamber is used in the simulations. For the

Table 2
Studied meshes and relative errors (RE) compared with the more refined mesh.

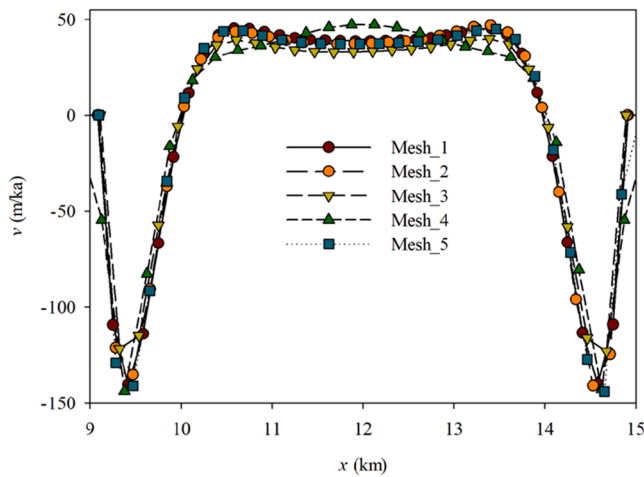| Mesh	X-Y nodes in chamber	Total nodes in chamber	RE
1	108×56	5832	0.0
2	96×48	4608	0.036
3	84×42	3528	0.071
4	72×36	2592	0.15
5 (Refi.)	88×44	3872	0.041

Fig. 2. Variation in *v*-velocity as a function of horizontal location in the magma chamber at the depth of its vertical center, $y = $ -4.5 km.

host rock a uniform mesh is used, which in all simulations is 120 × 60 nodes. This mesh study included both magma chamber and host rock.

4.3. Validation of the algorithm

The proposed mathematical model and algorithm is validated by comparing its results with experimental solidification data for pure gallium obtained by Gau and Viskanta (1986). Gallium is a widely studied metal, and the reference presents experimental results with cooling and solidification curves on the axis where gravity acts, which is essential for testing the approximation of the developed algorithm. The experimental study (Gau and Viskanta, 1986) examined the melting of pure gallium in a rectangular cavity with a laterally heated wall. A two-dimensional physical configuration for this case is inserted in Fig. 3. The dimensions of the mold are $\Delta x = 0.0889$ m and $\Delta y = \Delta x/2$. Constant temperatures of $T_{hot}(0,y,t) = 38.3°C$ and $T_{cold}(\Delta x, y, t) = 28.3°C$ at the lateral walls are imposed. The gallium is poured into the mold with an initial homogeneous temperature of $T_{cold} = 28.3°C$. Initial velocities in the computational domain are zero. The physical properties for pure gallium are listed in Table 3 (Gau and Viskanta, 1986).

The dimensionless mathematical model introduced in Section 2 was used to simulate the mathematical model and FVM proposed in this
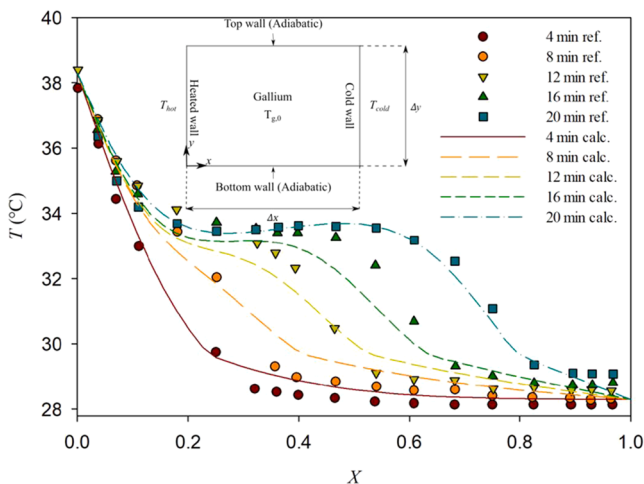

Fig. 3. Comparison between referenced results (Gau and Viskanta, 1986) and our calculated results for the gallium temperature profile at the centerline ($y = 0.022$) at different times. The schematic at the top was inserted to show the physical configuration used for the validation case.

Table 3
Gallium properties.

Liquid thermal conductivity (k_{sg})	32.0 W/ (m°C)
Solid thermal conductivity (k_{lg})	88.50 W/ (m°C)
Specific heat (Cp_g)	381.50 J/ (kg°C)
Latent heat (L_g)	80160.0 J/kg
Density of liquid phase (ρ_g)	6095.0 kg/m³
Dynamic viscosity of liquid phase (η_{lg})	1.81E-3 Pa s
Thermal expansion coefficient (β_g)	1.20E-4°C⁻¹
Melting temperature (T_{mg})	29.78°C

work. For this validation, the calculated domain was discretized with a uniform mesh of 44 × 22 nodes and a time step of 1.0E-3 s.

Fig. 3 presents a comparison between the experimental data (Gau and Viskanta, 1986) and our calculated results. It can be observed that the calculated results follow the trend obtained from the reference. The REs are 7.40E-3, 5.27E-3, 5.08E-3, 1.14E-2, and 1.31E-3 for 4 min, 8 min, 12 min, 16 min, and 20 min of cooling respectively, indicating a very good approximation.

## 5. Results for cooling of magma chambers and effects in host rock

This section presents two studies for the three shapes of rhyolitic magma chambers presented in Section 2.1 and shown in Fig. 1. Based on the assumptions and initial conditions detailed in previous sections, we first test the pure conductive cooling model, including the effect of latent heat. The results of the conduction model are compared with those obtained with the complete model of convection cooling presented in Section 3.4. The second study was designed to test the sensitivity of the solidification model when the range between "liquidus" (T_{lus}) and "solidus" (T_{sus}) temperature are varied. These studies do consider the effect of latent heat over the temperature range where crystallization occurs, and the effects of dehydration and decarbonation in the host rock that are lowering the melting temperature.

5.1. Cooling by means of conduction and convection models of melts

Several studies have considered only heat conduction in modeling the cooling of magma because the solution is much simpler than if convection is included (Paterson et al., 2011; Yoshinobu et al., 1998). This section compares the heat conduction model with the complete model of conduction-convection described in Section 3, which includes convection of the melt before and during the phase change (T_{lus}=725°C and T_{sus}=710°C).

The effect of phase change on magma cooling inside an enclosed magma chamber can be seen in the magma cooling curves of Fig. 4a for a temperature range between 800°C and 700°C for the three chamber shapes. The curves were obtained from a temperature (T) control point located in the center of the chamber (12 km, -4.5 km). In general, the comparison between the cooling curves using conduction and conduction-convection modeling shows that the conduction model has a longer cooling time. This agrees with previous studies on cooling cylindrical chambers as presented by Fu et al. (2010).

The curves begin when all magma is in the liquid phase. (Remember that the numerical procedure includes 6 ka of equilibration of the host rock during which the magma chamber has a constant temperature). In this first stage, temperature decreases from 800°C to 725°C (T_{lus}). This stage displays the first big difference when including convection in the crystallization process. The magma movement causes faster cooling in the middle of the chamber by transporting magma from the edges of the chamber towards the center; this happens constantly up to about 20 ka. After that, the cooling at the middle of the magma chamber slows down, because solidification begins at the boundaries of the magma chamber. The second part of the curve begins when the temperature of the control point reaches the liquidus temperature (T_{lus}=725°C). The slopes of the
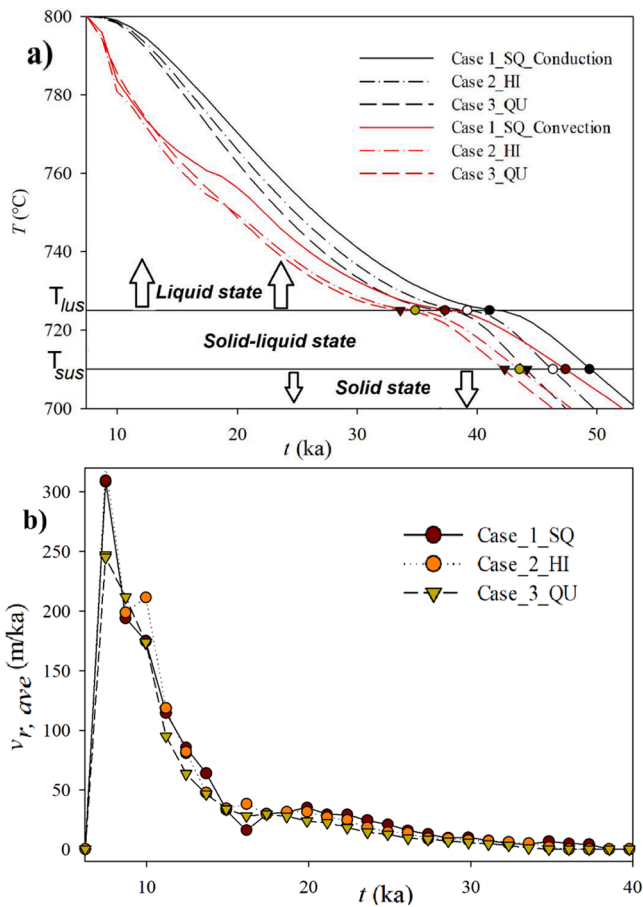
Fig. 4. (a) Results of modeling the cooling process inside the magma chambers for the three chamber shapes using conduction and conduction-convection models. Temperatures (*T*) are measurements at the middle point inside the magma chamber (*x* =12 km, *y* =-4.5 km). (b) Average of the absolute velocity vector inside the magma chamber using the convection model for the three shapes presented in this work.

curves change when crystals begin to form. In this second stage, temperature decreases from 725°C to 710°C over 7.5-10.1 ka for the conduction-convection model and 6.9-8.3 ka when the conduction-only model is used. Due to the position of the control point, at this time most of the magma in the chamber has crystallized and the temperatures for similar magma chamber cases tend to get closer. Below the "solidus" temperature (T_{sus}), the cooling continues until reaching thermal equilibrium with the environment (host rock). In this third and last part of the cooling curves, most of the magma in the chamber is in a solid state, hence the mathematical model in this part of the simulations is the same as for the conduction model. The temperature decreases slower for the conduction-convection models because temperature distributions around the control point are lower compared with those obtained with the conduction-only model.

Also, Fig. 4a displays cooling curves for the three simulated shapes of the magma chambers. Case 3 cools mostly quickly to the T_{lus}=725°C liquidus line and 700°C solidus line. Case 2 cools more slowly and case 1 is the slowest. This occurs in both conduction-only (black lines) and conduction-convection (red lines) models. The shape of the chamber affects the cooling time due to the varying surface area that is in contact with the host rock. This is because the host rock has different temperatures at different depths due to the temperature gradient, which causes the edges of the chamber to have different temperatures at different depths. For example, compared with cases 1 and 2, the quasi-elliptical chamber shape for case 3 has the smallest contact area with the deepest host rock where the temperature is highest. In consequence, the

major contact area with the host rock is at shallower depth where the host rock temperature is lower. This produces higher temperature gradients at the boundary for this case and therefore faster chamber cooling.

Fig. 4b presents the average velocity vectors in the melt for the three initial shapes of magma chambers. All cases display approximately the same trend. The melt begins to move by natural convection and its velocity increases to a maximum of 310 m/ka for cases 1 and 2 and 248 m/ka for case 3. The maximum value for the average velocity vector in all cases occurs at about 7.4 ka. After this, the velocities drop continuously until reaching zero.

Fig. 5 shows the temperature distribution and streamlines inside the magma chambers after 12.43 ka. The temperature distribution is influenced by the shape of the chamber. The isotherms in the liquid zone are affected slightly by the streamlines inside of the magma chamber. However, when the contour is below 750°C, the heat transfer looks like a conduction-only process despite convection being present for the cooling of the magma chamber, which is observed towards the boundaries of the chamber. In case 1, the streamlines are symmetric due to the rectangular geometry, but for cases 2 and 3 they are not symmetric because they are strongly affected by the magma chamber shape. The asymmetric convection patterns would transport crystals formed in different areas of the chamber at different temperatures in a way that may explain the variety of minerals that can be found in the same area of the chamber (Bartlett, 1969).

Fig. 6 shows the *v*-velocity profile at *v (x,* -4.5 km*)* for the three chamber shapes studied and at the same time (12.43 ka) as in Fig. 5. Observe that in all cases the maximum velocity values are positive and tend to be near the edges of the chamber. Positive velocity values indicate that the magma and formed crystals flow up in the chamber while negative values indicate that the magma flows downward. Note the symmetry of the *v*-velocity in case 1 with maximum values of 340 m/ka at *x* = 9.6 km and *x* = 14.6 km. Negative values are observed between *x* = 10 km and *x* = 14 km. In case 2 the maximum value of 480 m/ka is at *x* = 14.8 km. At this depth (*y* = -4.5 km), the negative or close to zero *v*-velocity values dominate towards the interior of the chamber. Case 3 shows lower *v*-velocity values compared to the previous cases. The maximum *v*-velocity of 132 m/ka are observed at *x* = 8.8 km, *x* = 11.5 km and *x* = 15.3 km.

5.2. Cooling by variation of the range between "solidus" and "liquidus" temperature

The crystallization temperature range varies with the geochemical composition of the magma (Nelson, 2011), so its definition and bounding limits are fundamental to understanding their effect on the magma crystallization process and the temperature distribution in the host rock. Magma can have a range of major element compositions depending on the fraction of melt from more mafic mantle or more felsic crustal source, as well as depending on partial melting, mixing, and fractional crystallization magmatic processes (Chappell, 1996). Although felsic melts can have a range of chemical compositions, in this work we assume that melt in the chamber has a very specific rhyolitic composition. Uncertainty about the crystallization range ($T_{range} = T_{lus}$ - T_{sus}) of rhyolitic magma is the result. Various authors indicate a range of 650−850°C for crystallization of felsic rhyolitic magmas, e.g., Nelson (Nelson, 2011). In this section, we test the sensitivity of the mathematical model by studying the effect of the crystallization range on magma cooling times. The results are obtained by setting the liquidus temperature at 725°C and varying the solidus temperature with three different values (T_{sus1} = 700°C, T_{sus2} = 710°C; and T_{sus3} = 718°C) giving ranges of T_{range1} =25°C, T_{range2} = 15°C and T_{range3} = 7°C. These temperature ranges are applied homogeneously for all melt in the chamber.

Fig. 7a shows the temporal evolution of magma cooling from 800°C to 640°C using the conduction-convection model and the three crystallization ranges indicated above. Temperatures (*T*) displayed were
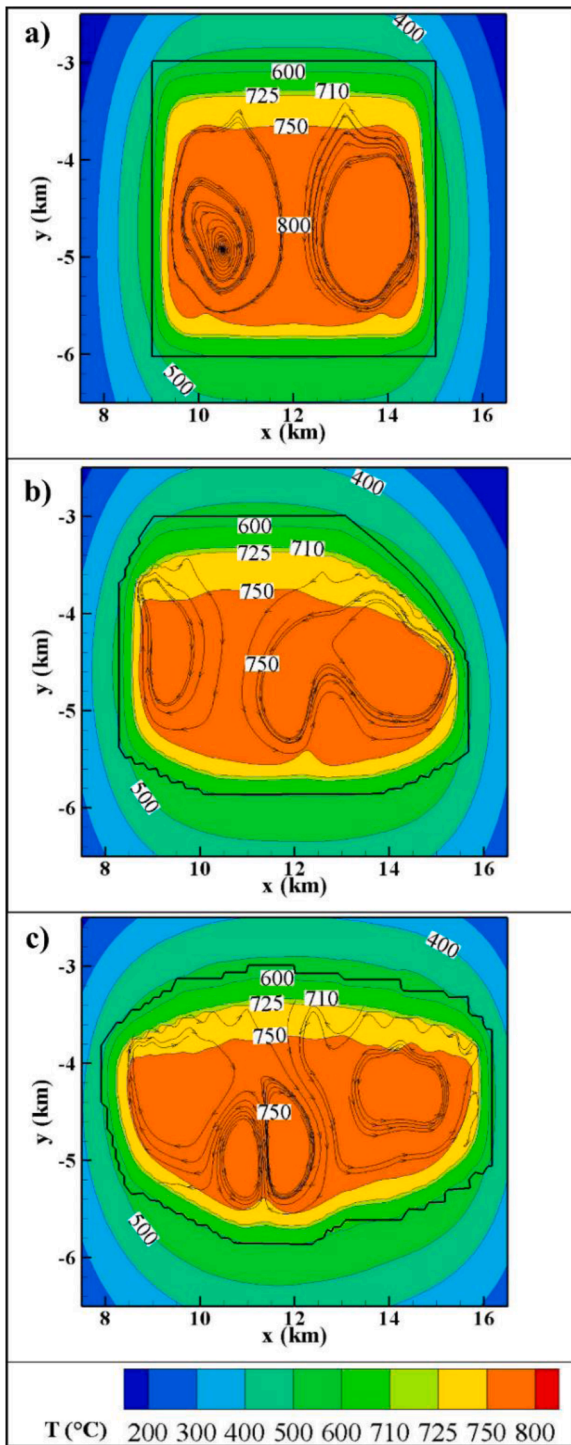
Fig. 5. Temperature distribution and streamlines after 12 ka for: a) case 1, b) case 2, and c) case 3. Note that liquidus T_{lus} =725°C and solidus T_{sus} = 710°C.

Fig. 6. Profile of v-velocity at (x, y = -4.5 km) inside the chamber at 12 ka for the three cases of chamber shape studied.
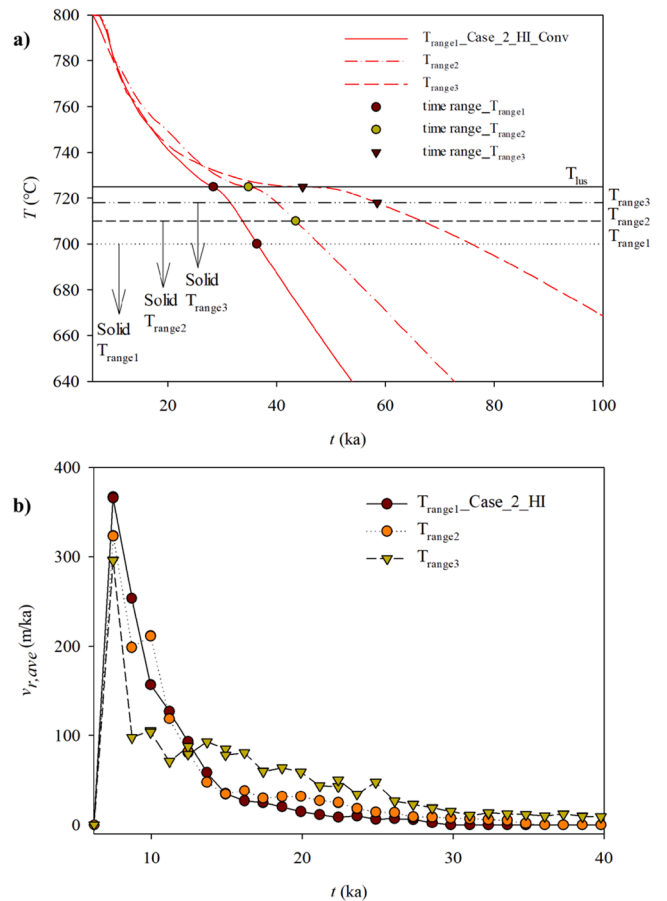
Fig. 7. (a) Temperature profile as a function of time for the conduction-convection model for three different crystallization temperature ranges. Temperature measurements (T) are at the middle point inside the magma chamber (x =12 km, y =-4.5 km). (b) Comparison of the average of the velocity vectors inside of the magma chamber for three crystallization temperature ranges. The results are obtained using the shape for case 2 and temperature ranges between solidus and liquidus of; T_{range1}=25°C, T_{range2}=15°C and T_{range3}=7°C.

calculated at the control point (12 km, -4.5 km) for the hybrid shape (case 2) which was chosen because it is intermediate between the ones used for cases 1 and 3. In the liquid stage of the cooling curve, the different temperature ranges produce different cooling times. This is because the temperatures shown are only for a point at the center of the chamber, but the solidification temperature ranges at the edges of the chamber are influencing the temperature changes in the center. When the range decreases, the core of the chamber takes longer to reach T_{lus} = 725°C. The time for crystallization from liquidus to solidus for T_{range1}, T_{range2}, and T_{renge3} are 8.0 ka, 8.67 ka and 13.71 ka, respectively. Total
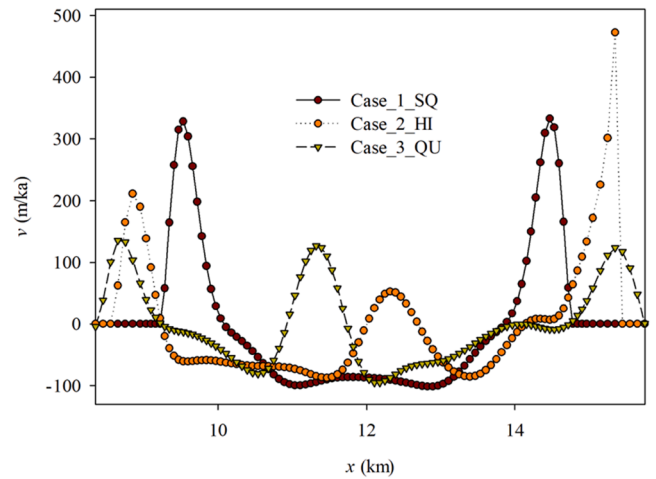
time for the chamber core to reach 670°C is 45 ka, 63 ka and 100 ka when using T_{range1}, T_{range2} and T_{range3} respectively.

In general, the total cooling time for the magma chamber contents

increases when the range in which crystals are forming in the melt is decreased. A decrease in temperature range over which the latent heat of crystallization acts is inversely proportional to the cooling rate of igneous bodies. This occurs due to the latent heat effect in the solidification zone which can increase the heat storage by one third in magmatic systems (Brikowski and Norton, 1989). This comes from comparing models with and without latent heat (Fu et al., 2010). It is understandable why this occurs from Eq. (5) of the mathematical model used in this work. The temperature range affects the stored heat in the phase change by augmenting the term L_m/T_{range} in the equation when the range decreases. Importantly, the latent heat of solidification decreases as the T_{range} increases. This is seen in the Fig. 7a cooling curve where the effect of latent heat is decreasing. This shows the importance of knowing the solidification temperature range of magmas, since it can significantly affect cooling estimates.

Fig. 7b shows the temporal evolution of the average velocity vectors inside a magma chamber for the case 2 hybrid shape using the three crystallization temperature ranges. The maximum average velocity resultant is always at the beginning of the cooling process when the magma is liquid, no matter the chamber shape (see Fig. 4b) or the solidification temperature range (see Fig. 7b).

Fig. 8 shows both the temperature distribution and streamlines inside a magma chamber for case 2 at 31.1 ka using three different solidification temperature ranges. The temperature decreases from the edges to the center with time. In places on the edges where the initial temperature of the host rock is higher, the temperature gradient is lower, and the magma loses heat more slowly. The temperature distribution and therefore the solidified zones follow the temperature contour lines. The different temperature distributions are a function of the different solidification temperature ranges. A decrease of the T_{range} results in slower dissipation of heat inside the magma chamber. At 31.1 ka no magma movement occurs by natural convection when the temperature range is $T_{range1} = 25°C$ (Fig. 8a), whereas movement still occurs when the range is T_{range2} (Fig. 8b) and T_{range3} (Fig. 8c). Fig. 8b shows a temperature contour line of intermediate thickness in the crystallization zone at $710°C < T < 725°C$ and a small liquid magma zone at the core of the chamber at $T > 725°C$. Fig. 8c shows a thin temperature layer at $718°C < T < 725°C$ and a large liquid magma zone at $T > 725°C$.

Both Figs. 5 and 8, show temperature distribution and streamlines. Notice that convection has no visible effect on the temperature distribution, and that the isotherm contour lines appear to display cooling by conduction only. This could be produced by both the low thermal diffusivity and high viscosity of the magma. The temperature distribution at different times shows that the contour lines are more widely spaced as the cooling process advances. The solidification temperature range affects the modeled cooling time. This is important in understanding zoning and crystal distribution in a pluton, since mineral transport inside a magma chamber resulting from convection is dependent on the cooling time.

5.3. Results for temperature histories as a function of time for a magma chamber

Fig. 9 shows both the magma chamber temperature and cooling rate curves as a function of time. The temperature is measured at the center of the magma chamber. The solidification temperature range is T_{range3}.

Fig. 9 shows how the magma chamber nucleus cools from 800 to 300°C over a time interval of 500 ka. Considering the magma chamber temperature as a function of time, three stages of the cooling process can be clearly seen: (1) liquid, (2) liquid-solid, and (3) solid. The liquid state has the highest temperature gradient between the magma chamber and the host rock, hence the cooling rate is highest and the cooling process fastest. The liquid-solid stage is where magma crystallization and mineralization occur and is the stage taking the least time in the cooling process. The cooling rate during the liquid-solid stage is minor, and the quantity of heat extracted during this stage can be attributed to the value
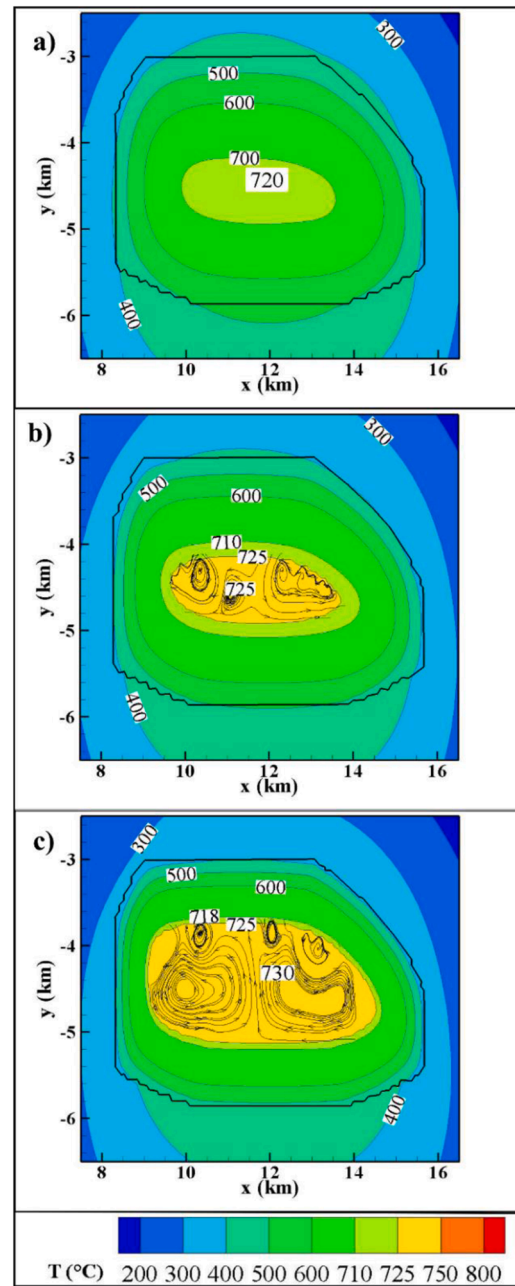

Fig. 8. Temperature distribution and streamlines at 31 ka for case 2 for: a) T_{range1}, b) T_{range2}, and c) T_{range3}.

of L_m. The solid stage is where the lowest temperature gradient between the magma chamber and the host rock exists, but is not the stage with the lowest cooling rate.

For the magma chamber cooling rate curve, the first liquid stage can be divided into two sub-stages for which two abrupt changes exist. The first sub-stage, which lasts from the start of cooling up to 10 ka, has the highest cooling rate between 2.8 and 14.0 ka and presumably, as seen in the previous sections, is mainly a stage of convection. Its average cooling rate is -6°C/ka (see Fig. 9). The second sub-stage that starts after 8.6 ka (see Fig. 9), initially has a slight increase in its heat transfer rate, but its decrease is fairly constant as it nears the liquid-solid stage. This probably occurs due to solidification of the magma chamber walls, as discussed in detail in previous sections. The cooling rate for this sub-stage ranges from 3°C/ka to 0.3°C/ka and its average cooling rate is 2°C/ka.

The liquid-solid stage begins after 35 ky with a very slow cooling rate (see Fig. 9) which slightly increases after 5 ky, presumably due to the
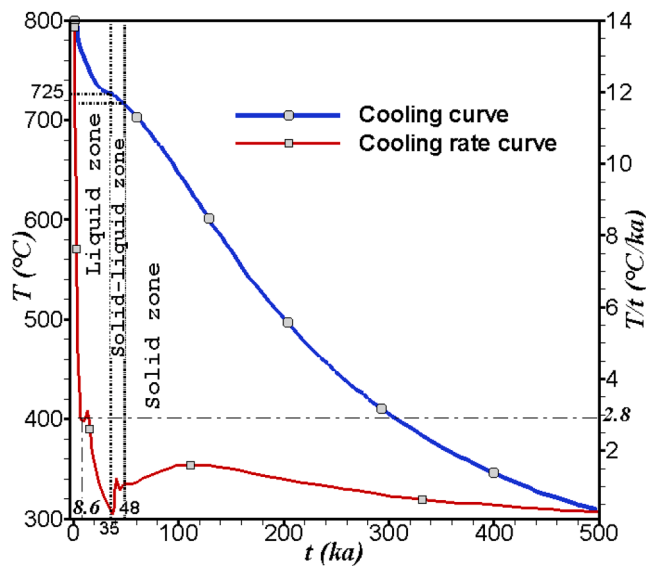
Fig. 9. Magma chamber cooling temperature (blue line) and cooling rate (red line) curves as a function of time. Temperatures are measured at the midpoint inside the magma chamber T ($x =12$ km, $y =-4.5$ km). (For interpretation of the references to color in this figure legend, the reader is referred to the web version of this article.)

presence of liquid magma inside. This results in convective heat transfer inside the magma chamber, hence, an increase in the cooling rate. After 40 ka, the cooling rate decreases slightly, because the magma slowly solidifies. As convection finishes (at 48 ky, see Fig. 9), cooling by conduction-only begins. Its average cooling rate is 0.88°C/ka.

Finally, the solid stage begins with a very small cooling rate that is quasi-constant, since the temperature gradient between the magma chamber and host rock progressively decreases. This work calculated the overall average cooling rate for the time interval shown in Fig. 9 as 1.02°C/ka. This occurs until the magma chamber and host rock reach thermal equilibrium. Then of course, the cooling rate goes to zero.

5.4. Results for the behavior of the host rock as a geothermal source

Tectonic subduction of the oceanic Nazca plate under the continental South American plate is the main factor causing magmatism in the region. Many geological faults associated with tectonism can be found in the Moquegua basin and its surroundings (Schildgen et al., 2009). Areas of high heat flow in southern Peru, as determined from temperature measurements at local wells by Hamza et al. (2005), coincide with active or Neogene volcanoes in southern of Peru (Japan International Cooperation Agency, 2012). Both magmatism and faults result in geothermal surface manifestations in the form of hot springs, mud pools, fumaroles and steam vents (Munoz, 2014). Therefore, geothermal prospecting in southern Peru should concentrate in an area with high heat flux that is close to an inactive or aseismic geological fault.

Determining the ground temperature in potential geothermal zones is one objective in the search for geothermal energy by exploration and drilling. Since the drilling phase is more expensive than exploration and drilling cost increases exponentially with depth (Rossi et al., 2020), having an accurate mathematical model for predicting the temperature distribution in the host rock becomes very relevant in the exploration phase. Such a model could significantly decrease the cost of the drilling phase. Our simulation does not include the water flux in the host rock, but it does include the heat flux from the chamber to a host rock made up of rock and water and the energy required for the water to evaporate, i. e., latent heat of evaporation. This provides a good approximation for the temperature distribution in the host rock above the magma chamber (Wang et al., 2012).

Fig. 10 a) shows the y temperature profile at $x =12$ km, the horizontal center of the magma chamber (case 2), at different times during the cooling process and for conduction and convection models. The temperature profile is shown to within 83 m of the surface. In the simulation, this is the position of the interior control volume nearest to the surface. Host rock temperatures are slightly lower during the first 62 ka when the magma conduction model is used. This is consistent with what is presented in Fig. 4 a), where it was shown that the conduction model has slower magma cooling times than the convection model. Our model coupled the temperatures of the chamber with those of the host rock, so it was expected that the conduction model would increase the temperature of the host rock more slowly.

Near-surface temperatures are 30°C, 40°C, 51°C, and 130°C after 12 ka, 31 ka, 62 ka, and 187 ka. When comparing the temperatures of the hot springs found in the Tacna area (Table 4) with those obtained near the surface, the simulation observes that they approximate those calculated between 62 ka and 187 ka. This indicates that the magma chambers that gave rise to these geothermal reservoirs could have between 62 ka and 187 ka since formation. A similar conclusion can be made by comparing the values of the temperature gradients obtained with the geothermometer presented in Table 4 (assuming a reservoir depth of 3 km) and those calculated from the data in Fig. 10a. On the other hand, it is interesting to observe the coincidence between the reservoir temperatures obtained using the Na-K-Mg geothermometer (Cruz et al., 2013) and those shown in Fig. 10 a), near the magma chamber. Also, these coincidences between the computational simulations and the field data indicate that the magma chambers that feed the geothermal zones of southern Peru may have a similar history to those that gave rise to the Peruvian coastal batholith.

Fig. 10 b) shows the temperature distribution at 62 ka for the host rock above a chamber with the shape of case 2 and T_{range2}. This Fig. provides the temperature distribution in the host rock between -3.8 km of depth and the surface. In the exploration of geothermal areas during the drilling phase, the information provided by the simulation plus the temperatures measured from wells drilled in the geothermal zone can be used to estimate the depth and shape of the magma chamber and in this way locate the best extraction point. For example, based on Fig. 10 b), if two test wells drilled to 2 km depth and spaced up to 2.0 km apart yield similar high temperatures (compared with other drilled wells in the area), it is possibly the top of a flat magma chamber. On the other hand, if the temperatures between two wells are greatly different, then it is possible that they are towards the sides of the magma chamber. Four or more temperature sets from wells drilled over a distance of 5 km at the surface could confirm the position and shape of the chamber in its upper area by measuring and comparing the temperature profiles between field data and simulation results.

Low- and high-grade temperatures used for geothermal energy are typically between 97°C and 210°C (Yekoladio et al., 2015; Zhang et al., 2018). A typical well hole can reach 2500 m depth (Espinoza-Ojeda et al., 2021) or more (DiPippo, 2016), but to generate electricity from geothermal energy, some drilling has been done down to 5-7 km deep (Rossi et al., 2020).

Fig. 11 shows the temperature profiles at y=-1.0, y=-2.5, and y=-5.0 km of depth for four different cooling times ($t_1 =12$ ka, $t_2 =31$ ka, $t_3 =62$ ka and $t_4 =187$ ka) and for a chamber in the shape of case 2 and T_{range2}. The range in the x-coordinate is taken from 0 to 8 km starting at the left edge of the computational control domain (see Fig. 1). In short, this figure presents a temperature profile at the side of the chamber at different times and depths. Maximum and minimum temperatures suggested to industrial geothermal exploitation are marked with red lines ($160 > T > 110$°C) (Yekoladio et al., 2015) in Fig. 11.

In general, temperatures in the host rock decrease with distance from the magma chamber and increase with the time. At 1 km of depth (Fig. 11 a) and after 187 ka of chamber cooling, temperatures in the optimal range for geothermal exploitation are founded between x=0 km to x=4.5 km. Cooling times below 62 ka present acceptable
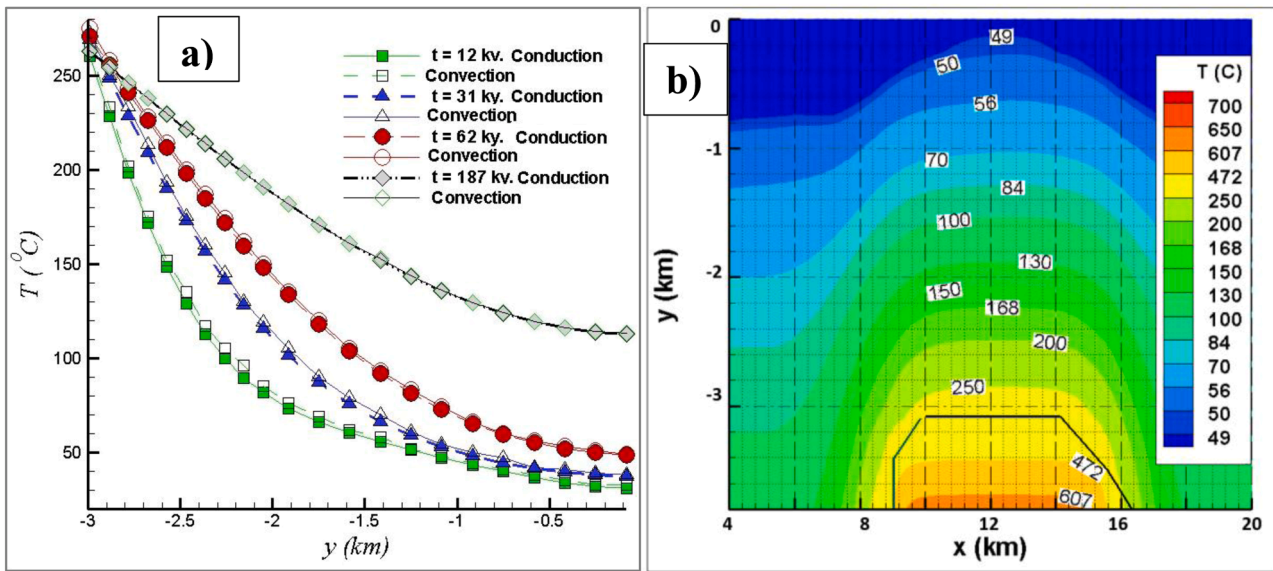
Fig. 10. (a) Temperature profiles in the host rock at $x = 12$ km for $-2.65 \leq y \leq -8.33E\text{-}2$ km at 12. ka, 31 ka, 62. ka, and 187 ka for the case 2 shape, using conduction and the conduction-advection model for the magma. (b) Temperature distribution in the chamber and host rock at 62 ka for the case 2 shape and T_{range2}.

Table 4

Temperatures measured from hot springs in geothermal areas near Tacna, Perú (Cruz et al., 2013). Table headings are maximum temperature at the surface ($T_{max,surf}$), reservoir temperature (RT) measured by geothermometer Na-K-Mg, temperature gradient (TG) assuming a reservoir depth of 3 km and a maximum temperature in range of RT, and calculated temperature gradient (TG_{calc}) at different times during the simulation (from Fig. 10a).

Geothermal Area	$T_{max,surf}$,°C	RT,°C	TG (°C/km)	Time (ka)	TG_{calc} (°C/km)
Tutupaca	61.9	≥185	63 (RT=200°C)	12	106
Calientes	86	240-280	65	31	98
Borateras	86	250-275	63	62	88
Ancocollo	85.6	180-280	65	187	56
Chungará-Kallapuma	61.9	250-275	71		

temperatures at short distance from the chamber and only after 31 ka of chamber cooling. At -2.5 km of depth (Fig. 11 b)) the x-distance to find temperatures in the optimal exploitation geothermal range are 0-4.1 km, 4.9-6.8 km, 6-7.4 km and 7.2-8 km for 187 ka, 62 ka, 31 ka and 12 ka, respectively. Clearly, at this depth finding optimum extraction points is more probable than at -1 km depth. Fig. 11c shows that at -5.0 km depth temperatures can always be found that can be used for geothermal energy ($T > 147°C$). A possible extraction zone located at 8-7 km from the edge of the magma chamber (x-position at 0-1 km) would be an ideal position, since for this depth at 187 ka the temperature will only vary around 10°. Temperatures below 160°C can be found for 12 ka at up to 2 km from the magma chamber.

Figs. 10 and 11 indicate that an ideal extraction zone could be located at -5 km of depth and 8 km from the magma chamber. This location of the extraction well would ensure a stable power supply for 180 ka. In general, temperatures are more stable over time in areas further away from the chamber. Temperatures of the host rock near the chamber can vary greatly in a short time. Therefore, geothermal energy extraction is not desirable from an extraction well near the magma chamber due to the high temperatures that the host rock can reach over time.

6. Conclusions

Our mathematical model shows good agreement in reproducing heat transfer phenomena that include the phase change. The simulation of a rhyolitic magma chamber under geological conditions yields results coherent with reference to the phase change from a liquid state to a solid state.

Our conclusions yield the factors affecting heat transfer and hence the cooling process of a magma chamber, listed here from most to least important: magma chamber shape, inclusion of convection in the cooling process, and solidification temperature range. The maximum magma velocity inside a chamber always occurs when the cooling process begins, and for the cases studied in this work it was 280 m/ka on average. Moreover, although the effect of convection is significant, the temperature distribution plot is similar to that for heat conduction. This is due to low thermal diffusivity and high viscosity. Note that both temperature distribution and streamlines are strongly linked to the shape of the magma chamber. Moreover, the temporal evolution of the temperature distribution shows the formation of crystallization zones and the evolution of its thickness with time, i.e., the crystallization zones become thicker with time. Therefore, the factors affecting the time for cooling a magma chamber, i.e., convection and solidification temperature range, are strongly linked. In addition, the quantity of liquid magma, the patterns of streamlines, and a changing velocity affect magma movement and change the location of minerals inside a magma chamber. This mathematical model can complement other studies concerning the behavior of magma in situations such as magmatic differentiation, epithermal deposits, and contact metamorphism.

When the convection-conduction and conduction-only models were compared, it was observed that the first simulates a faster cooling of the magma above the solidification temperature (T_{sus}). The higher rate of cooling in the magma chamber was found to produce slightly higher temperatures in the host rock around the chamber. Near the surface of the host rock, both models show similar effects on temperatures. From these results, it is possible to conclude that a conduction-only model is sufficient to calculate the heat fluxes and temperature distribution in a host rock surrounding a magma chamber; in addition, the solidification temperature range makes no difference. Knowing the temperature distribution at different depths in the host rock improves the probability of finding temperatures that can be used for geothermal energy based on geological and geophysical information. The use of mathematical
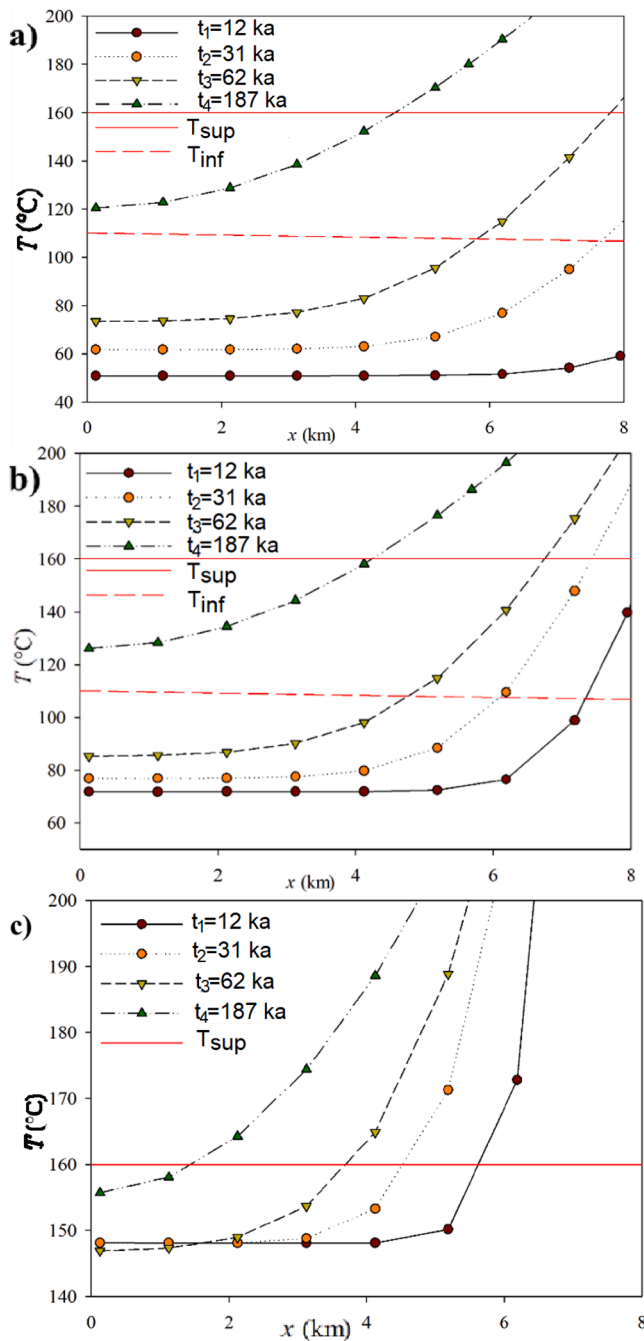
Fig. 11. Temperature profiles in the *x*-direction from the far-left edge of Fig. 1 at: (a) $y = -1.0$ km; (b) $y = -2.5$ km and (c) $y = -5.0$ km of depth in the host rock at 12 ka, 31 ka, 62 ka, and 187 ka for case 2 (T_{range2}). Red lines correspond to both superior and inferior temperature limits for the exploitation of geothermal energy ($160°$C, and $100°$C, respectively). (For interpretation of the references to color in this figure legend, the reader is referred to the web version of this article.)

models for computational simulation of geothermal reservoirs can contribute to the exploration phase, reducing the cost of the more expensive drilling phase. Temperatures useful for geothermal energy at up to 1 km depth are likely to be found. Moreover, the mathematical model can be inverted, using information about the temperature at different depths to determine the condition of the magma chambers at any time step. It is important to recognize the timescale for reaching the different cooling stages, and the fact that the temperature of the host rock remains fairly constant for thousands of years, allowing the use of

geothermal energy for a long time.

The conceptual model and the proposed simulations reproduce the activity of the geothermal zones of southern Peru. The results of the computational simulations indicate that the magma chambers that feed the geothermal areas of southern Peru may have a similar history to those that gave rise to the Peruvian coastal batholith.

Future work could describe the temperature and distribution of hydrothermal systems affected by heat fluxes from the magma chambers. Moreover, future work could study the relation between hydrothermal fluids and the ways to use geothermal energy, e.g., through organic Rankine cycles (ORCs), Combined Cooling, Heating and Power (CCHP) system, etc.

Code availability section

Name of the code/library

Contact: johan.gonzalez.novoa@gmail.com. Phone number +56949330584.

Hardware requirements: Windows 10 (any version) and Ram 2 gb.

Program language: Fortran 77.

Software required: Fortran 77 compiler and Tecplot 360 to visualize graphics results.

Program size: 68 kb.

The source codes are available for downloading at the link:

Code used to obtain validation results in section 7 can be obtained from:

Validation code

https://drive.google.com/file/d/10W43GY7bY0onrKz9thhUYqIt bRMUFekz/view?usp=sharing

Simple method

https://drive.google.com/file/d/1T51QVFdxba4-RZ0E2bMh pkxxF9h4gr0u/view?usp=sharing

Mesh generator

https://drive.google.com/file/d/1rHb-2_robdiTimtSpjHtLvYuAhqp PWhu/view?usp=sharing

Code used to obtain results in section 8 can be obtained from:

Square cavity, T_{range2}

https://drive.google.com/file/d/1PnZvGpEXXx2tVeMzfe aG0tZJANnYry31/view?usp=sharing

Hybrid cavity, T_{range2}

https://drive.google.com/file/d/1MJfT2GYCZ7Ydg2vjF 2H9mkb8L2Sj_mWo/view?usp=sharing

Quasi-elliptical cavity T_{range2}

https://drive.google.com/file/d/1lyARNH7CVQ649zhQz s-NcKvMcdSvenTz/view?usp=sharing

Hybrid cavity, T_{range1}

https://drive.google.com/file/d/1fzCtW-fITCyDDIvYMtQgVm32a0_ JgwFe/view?usp=sharing

Hybrid cavity, T_{range3}

https://drive.google.com/file/d/1s5DXzIx6LR82m8oaEjIivCFbJCE HdaOZ/view?usp=sharing

Simple method

https://drive.google.com/file/d/1T51QVFdxba4-RZ0E2bMh pkxxF9h4gr0u/view?usp=sharing

Mesh generator

https://drive.google.com/file/d/1rHb-2_robdiTimtSpjHtLvYuAhqp PWhu/view?usp=sharing

CRediT authorship contribution statement

Johan González: Conceptualization. **Carlos E. Zambra:** Conceptualization, Methodology, Software, Formal analysis, Resources, Project administration, Writing – review & editing, Supervision. **Luciano González:** Methodology, Software, Validation, Formal analysis, Writing – original draft, Visualization. **Benjamin Clausen:** Investigation, Funding acquisition, Writing – review & editing. **Diego A. Vasco:**

Writing – review & editing.

Declaration of Competing Interest

The authors declare that they have no known competing financial interests or personal relationships that could have appeared to influence the work reported in this paper.

Acknowledgments

References

Agar, R.A., 1981. Copper mineralization and magmatic hydrothermal brines in the Rio Pisco section of the Peruvian coastal batholith. Econ. Geol. 76, 677–693. https://doi.org/10.2113/gsecongeo.76.3.677.

Ahlers, G., Grossmann, S., Lohse, D., 2009. Heat transfer and large scale dynamics in turbulent Rayleigh-Bénard convection. Rev. Mod. Phys. 81, 503–537. https://doi.org/10.1103/RevModPhys.81.503.

Alván, A.A., Bustamante, Y.F., Sánchez, E.A., Mamani, M.I., 2020. Stratigraphic architecture, paleogeography and provenance of the cenozoic sedimentary rocks in southern perú (Tacna, 18° s). Andean Geol. 47, 351–383. https://doi.org/10.5027/andgeov47n2-3168.

Barragán, R.M., Arellano, V.M.G., Birkle, P., Portugal, E.M., Díaz, G.H., 1999. Chemical description of spring waters from the Tutupaca and Rio Calientes (Peru) geothermal zones. Int. J. Energy Res. 23, 125–139. https://doi.org/10.1002/(sici)1099-114x(199902)23:2<125::aid-er466>3.0.co;2-r.

Bartlett, R.W., 1969. Magma convection, temperature distribution, and differentiation. Am. J. Sci. 267, 1067–1082. https://doi.org/10.2475/ajs.267.9.1067.

Brikowski, T., Norton, D., 1989. Influence of magma chamber geometry on hydrothermal activity at mid-ocean ridges. Earth Planet. Sci. Lett. 93, 241–255. https://doi.org/10.1016/0012-821X(89)90072-1.

Chappell, B.W., 1996. Magma mixing and the production of compositional variation within granite suites: evidence from the granites of southeastern Australia. J. Petrol. 37, 449–470. https://doi.org/10.1093/petrology/37.3.449.

Cobbing, J., Garayar, J., 1998. Mapa Geológico del Cuadrángulo de Oyón (22j) [WWW Document]. Servicio de Geología y Minería, República del Perú. URL https://hdl.handle.net/20.500.12544/2166 (accessed 2.28.22).

Couch, R., Whitsett, R., Huehn, B., Briceno-Guarupe, L., 1981. Structures of the continental margin of Peru and Chile. Memoir Geol. Soc. Am. 154, 703–726. https://doi.org/10.1130/MEM154-p703.

Cruden, A.R., 1998. On the emplacement of tabular granites. J. Geol. Soc. Lond. 155, 853–862. https://doi.org/10.1144/gsjgs.155.5.0853.

Cruz Pauccara, V., Guardia, Xi, 2015. Geothermal Country Update for Peru, 2010-2014. World Geotermal Congress 2015, Melbourne, Australia, p. 9.

Cruz, V., Vargas, V., Cacya, L., 2013. Caracterización y Evolución del Potencial Geotérmico de la Región de Tacna. INGEMMET.

Davies, J.H., Davies, D.R., 2010. Earth's surface heat flux. Solid Earth 1, 5–24. https://doi.org/10.5194/se-1-5-2010.

Deb, P., Giordano, G., Shi, X., Lucci, F., Clauser, C., 2021. An approach to reconstruct the thermal history in active magmatic systems: Implications for the Los Humeros volcanic complex, Mexico. Geothermics 96, 102162. https://doi.org/10.1016/j.geothermics.2021.102162.

DiPippo, R., 2016. Exploration strategies and techniques. Geothermal Power Plants. Elsevier, pp. 23–47. https://doi.org/10.1016/B978-0-08-100879-9.00002-1.

Douglas, M.M., Geyer, A., Álvarez-Valero, A.M., Martí, J., 2016. Modeling magmatic accumulations in the upper crust: metamorphic implications for the country rock. J. Volcanol. Geotherm. Res. 319, 78–92. https://doi.org/10.1016/j.jvolgeores.2016.03.008.

Eckert, E.R.G., Goldstein, R.J., Pfender, E., Ibele, W.E., Patankar, S.V., Ramsey, J.W., Simon, T.W., Decker, N.A., Kuehn, T.H., Lee, H., Girshick, S.L., 1988. Heat transfer—a review of 1987 literature. Int. J. Heat Mass Transf. 31, 2401–2488. https://doi.org/10.1016/0017-9310(88)90174-3.

Espinoza-Ojeda, O.M., Macías, J.L., Gómez-Arias, E., Muñiz-Jauregui, J.A., Rivera-Calderón, E., Figueroa-Soto, A.G., Vázquez-Rosas, R., Garduño-Monroy, V.H., 2021. A two-dimensional temperature field simulation of the La Primavera geothermal area, México. Geothermics 96. https://doi.org/10.1016/j.geothermics.2021.102201.

Fjeldskaar, W., Helset, H.M., Johansen, H., Grunnaleite, I., Horstad, I., 2008. Thermal modelling of magmatic intrusions in the Gjallar Ridge, Norwegian Sea: implications for vitrinite reflectance and hydrocarbon maturation. Basin Res. 20, 143–159. https://doi.org/10.1111/j.1365-2117.2007.00347.x.

Fu, F.Q., McInnes, B.I.A., Evans, N.J., Davies, P.J., 2010. Numerical modeling of magmatic-hydrothermal systems constrained by U-Th-Pb-He time-temperature histories. J. Geochem. Explor. 106, 90–109. https://doi.org/10.1016/j.gexplo.2009.09.001.

Galushkin, Y.I., 1997. Thermal effects of igneous intrusions on maturity of organic matter: a possible mechanism of intrusion. Org. Geochem. 26, 645–658. https://doi.org/10.1016/S0146-6380(97)00030-2.

Gau, C., Viskanta, R., 1986. Melting and solidification of a pure metal on a vertical wall. J. Heat Transf. 108, 174–181. https://doi.org/10.1115/1.3246884.

González Olivares, L.U, 2017. Conduction Plus Convection Heat Flow Modeling for the Linga Complex. Peruvian Coastal Batholith. Loma Linda University.

González-Acevedo, Z.I., García-Zarate, M.A., 2019. Geothermal energy as an alternative to reduce atmospheric emissions and provide green energy. Green Technologies to Improve the Environment on Earth. IntechOpen, p. 13. https://doi.org/10.5772/intechopen.80759.

Gudmundsson, A., 2012. Magma chambers: Formation, local stresses, excess pressures, and compartments. J. Volcanol. Geotherm. Res. https://doi.org/10.1016/j.jvolgeores.2012.05.015.

Guo, Q., Fink, R., Littke, R., Zieger, L., 2019. Methane sorption behaviour of coals altered by igneous intrusion, South Sumatra Basin. Int. J. Coal Geol. 214, 103250 https://doi.org/10.1016/j.coal.2019.103250.

Haederle, M., Atherton, M.P., 2002. Shape and intrusion style of the Coastal Batholith. Peru. Tectonophys. 345, 17–28.

Hamza, V.M., Dias, F.J.S.S., Gomes, A.J.L., Terceros, Z.G.D., 2005. Numerical and functional representations of regional heat flow in South America. Phys. Earth Planet. Interfaces 152, 223–256. https://doi.org/10.1016/j.pepi.2005.04.009.

Hayba, D.O., Ingebritsen, S.E., 1997. Multiphase groundwater flow near cooling plutons. J. Geophys. Res. 12235–12252.

Iyer, K., Svensen, H., Schmid, D.W., 2018. SILLi 1.0: a 1-D numerical tool quantifying the thermal effects of sill intrusions. Geosci. Model Dev. 11, 43–60. https://doi.org/10.5194/gmd-11-43-2018.

Japan International Cooperation Agency, J., 2012. The Master Plan for development of geothermal energy in Peru: Final Report.

Kaminski, E., Jaupart, C., 2003. Laminar starting plumes in high-Prandtl-number fluids. J. Fluid Mech. 478, 287–298. https://doi.org/10.1017/S0022112002003233.

Keller, T., Suckale, J., 2019. A continuum model of multi-phase reactive transport in igneous systems. Geophys. J. Int. 219, 185–222. https://doi.org/10.1093/gji/ggz287.

Lamy-Chappuis, B., Heinrich, C.A., Driesner, T., Weis, P., 2020. Mechanisms and patterns of magmatic fluid transport in cooling hydrous intrusions. Earth Planet. Sci. Lett. 535, 116111 https://doi.org/10.1016/j.epsl.2020.116111.

Lesher, C.E., Spera, F.J., 2015. Thermodynamic and transport properties of silicate melts and magma. The Encyclopedia of Volcanoes. Elsevier, pp. 113–141. https://doi.org/10.1016/B978-0-12-385938-9.00005-5.

Liu, H., Jiang, B., 2019. Differentiated evolution of coal macromolecules in localized igneous intrusion zone: a case study of Zhuxianzhuang colliery, Huaibei coalfield, China. Fuel 254, 115692. doi:10.1016/j.fuel.2019.115692.

Llambías, E.J., 2014. Geología de los Cuerpos Igneos - CAPITULO 1 [WWW Document].

Lowell, R.P., Kolandaivelu, K., Rona, P.A., 2014. Hydrothermal activity ☆. Reference Module in Earth Systems and Environmental Sciences 1–19. https://doi.org/10.1016/B978-0-12-409548-9.09132-6.

Lund, J.W., 2007. Characteristics, development and utilization of geothermal resources. In: ISES Solar World Congress 2007, ISES, 1, pp. 87–95. https://doi.org/10.1007/978-3-540-75997-3_13.

Moraga, N.O., Andrade, M.A., Vasco, D.A., 2010. Unsteady conjugate mixed convection phase change of a power law non-Newtonian fluid in a square cavity. Int. J. Heat Mass Transf. 53, 3308–3318. https://doi.org/10.1016/j.ijheatmasstransfer.2010.02.044.

Nelson, S.a, 2011. Magmas and igneous rocks. In: Earth & Environmental Sciences 1110 Physical Geology, pp. 1–14.

Ni, H., Hui, H., Steinle-Neumann, G., 2015. Transport properties of silicate melts. Rev. Geophys. 53, 715–744. https://doi.org/10.1002/2015RG000485.

Patankar, S. V., 1980. Numerical heat transfer and fluid flow.

Paterson, S.R., Okaya, D., Memeti, V., Economos, R., Miller, R.B., 2011. Magma addition and flux calculations of incrementally constructed magma chambers in continental margin arcs: combined field, geochronologic, and thermal modeling studies. Geosphere 7, 1439–1468. https://doi.org/10.1130/GES00696.1.

Rabbanipour Esfahani, B., Hirata, S.C., Berti, S., Calzavarini, E., 2018. Basal melting driven by turbulent thermal convection. Phys. Rev. Fluids 3, 053501. https://doi.org/10.1103/PhysRevFluids.3.053501.

Rad, M.T., Kotas, P., Beckermann, C., 2013. Rayleigh number criterion for formation of a-segregates in steel castings and ingots. Metall. Mater. Trans. A 44, 4266–4281. https://doi.org/10.1007/s11661-013-1761-4.

Ramirez, J.C., Beckermann, C., 2003. Evaluation of a rayleigh-number-based freckle criterion for Pb-Sn alloys and Ni-base superalloys. Metall. Mater. Trans. A 34, 1525–1536. https://doi.org/10.1007/s11661-003-0264-0.

Rossi, E., Jamali, S., Saar, M.O., Rudolf von Rohr, P., 2020. Field test of a Combined Thermo-Mechanical Drilling technology. Mode I: Thermal spallation drilling. J. Pet. Sci. Eng. 190, 107005 https://doi.org/10.1016/j.petrol.2020.107005.

Ryerson, F.J., Weed, H.C., Piwinskii, A.J., 1988. Rheology of subliquidus magmas: 1. Picritic compositions. J. Geophys. Res. 93, 3421. https://doi.org/10.1029/JB093iB04p03421.

Sanders, L., 1998. A Manual of Field Hydrogeology. Prentice Hall. https://doi.org/10.1038/099523b0.

Schildgen, T.F., Hodges, K.V., Whipple, K.X., Pringle, M.S., Van Soest, M., Cornell, K., 2009. Late cenozoic structural and tectonic development of the western margin of the central andean plateau in southwest Peru. Tectonics 28, 1–21. https://doi.org/10.1029/2008TC002403.

Shaw, H.R., 1965. Comments on viscosity, crystal settling, and convection in granitic magmas. Am. J. Sci. 263, 120–152. https://doi.org/10.2475/ajs.263.2.120.

Shaw, H.R., Wright, T.L., Peck, D.L., Okamura, R., 1968. The viscosity of basaltic magma; an analysis of field measurements in Makaopuhi lava lake, Hawaii. Am. J. Sci. 266, 225–264. https://doi.org/10.2475/ajs.266.4.225.

Sonder, I., Zimanowski, B., Büttner, R., 2006. Non-Newtonian viscosity of basaltic magma. Geophys. Res. Lett. 33, L02303. https://doi.org/10.1029/2005GL024240.

Sparks, R.S.J., Annen, C., Blundy, J.D., Cashman, K.V., Rust, A.C., Jackson, M.D., 2019. Formation and dynamics of magma reservoirs. Philos. Trans. R. Soc. A 377, 20180019. https://doi.org/10.1098/rsta.2018.0019.

Sparks, R.S.J., Huppert, H.E., Turner, J.S., Sakuyama, M., O'Hara, M.J., 1984. The fluid dynamics of evolving magma chambers [and Discussion]. Philos. Trans. R. Soc. A 310, 511–534. https://doi.org/10.1098/rsta.1984.0006.

Vargas, L., Del Pino, M., 1995. Mapa Geológico del Cuadrángulo de Arequipa. Departamento de Arequipa (33-s).

Versteeg, H.M., Malalasekera, W., 2007. An Introduction to Computational Fluid Dynamics: the Finite Volume Method, second ed. Prentice Hall, Harlow.

Wang, D., Song, Y., Liu, Y., Zhao, M., Qi, T., Liu, W., 2012. The influence of igneous intrusions on the peak temperatures of host rocks: finite-time emplacement, evaporation, dehydration, and decarbonation. Comput. Geosci. 38, 99–106. https://doi.org/10.1016/j.cageo.2011.05.011.

Yekoladio, P.J., Bello-Ochende, T., Meyer, J.P., 2015. Thermodynamic analysis and performance optimization of organic rankine cycles for the conversion of low-to-moderate grade geothermal heat. Int. J. Energy Res. 39, 1256–1271. https://doi.org/10.1002/er.3326.

Yoshinobu, A.S., Okaya, D.A., Paterson, S.R., 1998. Modeling the thermal evolution of fault-controlled magma emplacement models: implications for the solidification of granitoid plutons. J. Struct. Geol. 20, 1205–1218. https://doi.org/10.1016/S0191-8141(98)00064-9.

Zambra, C.E., Gonzalez-Olivares, L., González, J., Clausen, B., 2022. Temporal evolution of cooling by natural convection in an enclosed magma chamber. Processes 10. https://doi.org/10.3390/pr10010108.

Zambra, C.E., Muñoz, J.F., Moraga, N.O., 2015. A 3D coupled model of turbulent forced convection and diffusion for heat and mass transfer in a bioleaching process. Int. J. Heat Mass Transf. 85, 390–400. https://doi.org/10.1016/j.ijheatmasstransfer.2015.01.135.

Zhang, C., Jiang, G., Shi, Y., Wang, Z., Wang, Y., Li, S., Jia, X., Hu, S., 2018. Terrestrial heat flow and crustal thermal structure of the Gonghe-Guide area, northeastern Qinghai-Tibetan plateau. Geothermics 72, 182–192. https://doi.org/10.1016/j.geothermics.2017.11.011.